Forschungszentrum Karlsruhe
in der Helmholtz-Gemeinschaft

Wissenschaftliche Berichte
FZKA 7118

Modelling of B_4C Oxidation by Steam at High Temperatures Based on Separate-effects Tests and its Application to the Bundle Experiment QUENCH-07

M.S. Veshchunov, A.V. Berdyshev, A.V. Boldyrev, A.V. Palagin, V.E. Shestak, M. Steinbrück, J. Stuckert

Institut für Materialforschung
Programm Nukleare Sicherheitsforschung

Juni 2005

Impressum der Print-Ausgabe:

Als Manuskript gedruckt

Forschungszentrum Karlsruhe GmbH
Postfach 3640, 76021 Karlsruhe

Mitglied der Hermann von Helmholtz-Gemeinschaft
Deutscher Forschungszentren (HGF)

ISSN 0947-8620

urn:nbn:de:0005-071188

Forschungszentrum Karlsruhe

in der Helmholtz-Gemeinschaft

Wissenschaftliche Berichte

FZKA 7118

Modelling of B_4C oxidation by steam at high temperatures based on separate-effects tests and its application to the bundle experiment QUENCH-07

M.S. Veshchunov*, A.V. Berdyshev*, A.V. Boldyrev*, A.V. Palagin*, V.E. Shestak*, M. Steinbrück, J. Stuckert

Institut für Materialforschung

Programm Nukleare Sicherheitsforschung

* IBRAE, Moscow

Forschungszentrum Karlsruhe GmbH, Karlsruhe

2005

Zusammenfassung

Entwicklung eines Modells zur Oxidation von B_4C in Dampf bei hohen Temperaturen auf der Basis von Einzeleffektuntersuchungen und Anwendung auf das Bündelexperiment QUENCH-07

Basierend auf Einzeleffektuntersuchungen in der FZK BOX-Anlage wurde bei IBRAE, Moskau, ein Modell zur Beschreibung der Oxidation von B_4C bei hohen Temperaturen entwickelt. Das Modell berücksichtigt die Reaktionskinetik an der Probenoberfläche und den Massetransport in der Gasphase als geschwindigkeitsbestimmende Mechanismen.

Das Modell beinhaltet den kompletten Satz unabhängiger chemischer Reaktionen bei der Oxidation von Borkarbid sowie einen kompletten Satz von Gleichungen für das Massenwirkungsgesetz in der Gasphase.

Im Gegensatz zu anderen Modellansätzen wurde hier für die Nichtgleichgewichtsreaktionen an der Oberfläche aus den BOX-Experimenten eine semi-empirische Korrelation für die Reaktionsrate ermittelt. Dieses Vorgehen erlaubt eine genauere Berechnung der Freisetzungsraten von Wasserstoff und anderen Gasen bei der Oxidation von Borkarbid.

Das neue Modell wurde in den SVECHA/QUENCH (S/Q) Code implementiert und an den BOX-Ergebnissen verifiziert.

Weiterhin wurde der S/Q Code zur Simulation des QUENCH-07 Experiments mit B_4C Absorberstab angewandt. Dazu wurde das "effective channel" Modell verwendet und zur Berechnung der Gasfreisetzung im Bündel angewandt.

Das neue Modell steht zur Implementierung in andere Computerprogramme zur Simulation schwerer Störfälle zur Verfügung, eine vereinfachte Version wurde bereits mit guten Ergebnissen in den russischen Störfall-Code RATEG/SVECHA eingebaut.

Contents

List of Tables 5
List of Figures 6
1. Introduction 9
2. Main dependencies of B_4C oxidation kinetics revealed in BOX Rig tests 9
2.1. Test conduct and observations 9
2.2. Dependence of B_4C oxidation rate on gas dynamic conditions 12
2.3. Dependence of B_4C oxidation rate on steam partial pressure 13
2.4. Temperature dependence of B_4C oxidation rate 16
3. Modelling approach to B_4C oxidation by steam 18
3.1. Main chemical processes at the reaction interface 18
3.2. Flux matches at the B_4C/gas interface and in the gas bulk 21
3.3. Diffusion fluxes in the gas boundary layer 22
3.3.1. Viscosity of gas mixture 23
3.3.2. Gas diffusion coefficients in gas mixture 24
3.4. Complete set of equations 24
3.5. Model implementation in the SVECHA/QUENCH code 26
4. Verification of B_4C oxidation model against BOX Rig tests 28
4.1. Fitting of model parameters against isothermal tests 28
4.2. Verification against tests with varying atmosphere 31
4.3. Verification against isothermal tests with reduced steam flow rate 33
4.4. Verification against transient temperature tests 35
4.5. Verification against measurements of minor gaseous products release 36
4.6. Heat effect of B_4C oxidation 42
5. Model predictions for future tests 46
5.1. Determination of various kinetic regimes 46
5.2. Methane generation on cool-down of the outlet reaction gas mixture 48
6. Application of the SVECHA/QUENCH code with the newly implemented B_4C oxidation model to simulation of the QUENCH-07 bundle test 49
6.1. QUENCH-07 bundle test 49
6.2. Effective channel approach 49
6.3. Processing of the QUENCH-07 bundle test temperature data 50
6.4. QUENCH-07 bundle test simulation with Zr/ZrO_2 central rod 51
6.5. QUENCH-07 bundle test simulation with B_4C central rod 53
6.6. Main outcomes 57
7. Conclusions 57
Acknowledgements 58

Appendix 1. Justification of a weak dependence of the oxidation rate on diffusion rate in the liquid B_2O_3 layer 59

References 61

List of Tables

Table 1: B_4C specimens used in BOX experiments

Table 2: Test parameters of experiments on B_4C oxidation in the BOX Rig at 1200°C

Table 3: Tests under varying steam production rate (Box 10115)

Table 4: Tests under varying argon flow rate (Box 10126)

Table 5: Summary of test results (Box 10115 and Box 10126)

Table 6: Parameters A and m for different Reynolds numbers.

Table 7: Standard viscosity and Saterland's constant for steam and argon.

Table 8: Parameters of binary diffusion for gas mixtures.

Table 9: Values of critical volumes.

Table 10: Test conditions and results of isothermal tests on B_4C oxidation in the BOX Rig. Steam flow rate of 30 g/h and argon flow rate of 50 l/h

Table 11: Test conditions of tests on B_4C oxidation in the BOX Rig under varying steam or argon flow rates.

Table 12: Test conditions and results of isothermal experiments on B_4C oxidation in the BOX Rig under reduced steam flow rate of 3 g/h and argon flow rate of 50 l/h.

Table 13: Test conditions of transient temperature test on B_4C oxidation in the BOX Rig in argon/steam mixture.

Table 14: Total amount of different components released during the test.

List of Figures

Fig. 1: Hydrogen release during isothermal oxidation of various specimens at 1200°C:.

Fig. 2: Pre-test mass (black), post-test mass (red), B_2O_3 formed, recalculated from the hydrogen release data (green), and B_2O_3 remaining in the specimen, calculated as the difference between post-test mass and oxidised B_4C (blue) for the various specimens, in dependence on temperature (from [1]).

Fig. 3: Oxidation of B_4C specimens at T=1400°C.

Fig. 4: B_4C specimen support for scoping tests (top) and improved version (bottom).

Fig. 5: Influence of steam (a) and argon (b) flow rate on oxidation kinetics at 1200°C.

Fig. 6: Dependence of hydrogen release rate on bulk steam partial pressure. Compilation of Box 10115 and Box 10126 test data.

Fig. 7: Calculated specific reaction rate $\alpha(T) = W(P_{H_2O}, T) / P_{H_2O}$ as function of temperature.

Fig. 8: Schematic representation of total complex reaction rate as function of temperature. Curves 1 and 2 represent two parallel stages.

Fig. 9: Schematic representation of the model.

Fig. 10: Schematic representation of the model implemented in the S/Q code.

Fig. 11: Measured hydrogen release rate during isothermal oxidation of different type of B_4C pellet for the case of steam flow rate of 30 g/h and argon flow rate of 50 l/h.

Fig. 12: S/Q simulation of hydrogen release rate during isothermal oxidation of Framatome B_4C pellet for the case of steam flow rate of 30 g/h and argon flow rate of 50 l/h.

Fig. 13: Comparison of measured and S/Q simulation results of hydrogen release rate during isothermal oxidation of different type of B_4C pellet for the case of steam flow rate of 30 g/h and argon flow rate of 50 l/h.

Fig. 14: Comparison of measured and S/Q simulation results for hydrogen release rate during oxidation of Framatome B_4C pellet at 1200°C in argon/steam in the test BOX 10115. Variation of steam flow rate.

Fig. 15: Comparison of measured and S/Q simulation results for hydrogen release rate during oxidation of Framatome B_4C pellet at 1200°C in argon/steam in the test BOX 10126. Variation of argon flow rate.

Fig. 16: Comparison of measured and S/Q simulation results for hydrogen release rate during isothermal oxidation of Framatome and ESK B_4C pellets for the case of reduced steam flow rate of 3 g/h and argon flow rate of 50 l/h.

Fig. 17: Test conditions and measured gas release rate in the test BOX 10406. Transient temperature oxidation of Framatome B_4C pellet under steam flow rate of 30 g/h and argon flow rate of 50 l/h.

Fig. 18: Comparison of measured and S/Q simulation results for hydrogen release rate during transient temperature oxidation of Framatome B_4C pellet in the test BOX 10406.

Fig. 19: Comparison of measured and S/Q simulation results for the carbon dioxide steady-state release rate during isothermal oxidation of different types of B_4C pellets for the case of steam flow rate of 30 g/h and argon flow rate of 50 l/h.

Fig. 20: Comparison of measured and S/Q simulation results for the carbon monoxide steady-state release rate during isothermal oxidation of different types of B_4C pellets for the case of steam flow rate of 30 g/h and argon flow rate of 50 l/h.

Fig. 21: Comparison of measured and S/Q simulation results for the methane steady-state release rate during isothermal oxidation of different types of B_4C pellets for the case of steam flow rate of 30 g/h and argon flow rate of 50 l/h.

Fig. 22: S/Q simulation of the orthoboric (H_3BO_3) and metaboric (HBO_2) acids steady-state release rates during isothermal oxidation of B_4C pellets for the case of steam flow rate of 30 g/h and argon flow rate of 50 l/h.

Fig. 23: S/Q simulation of the boron oxide (B_2O_3) and the trimer of metaboric acid ($H_3B_3O_6$) steady-state release rates during isothermal oxidation of B_4C pellets for the case of steam flow rate of 30 g/h and argon flow rate of 50 l/h.

Fig. 24: Comparison of measured and S/Q simulation results for the carbon dioxide steady-state release rate during isothermal oxidation of Framatome and ESK B_4C pellets for the case of reduced steam flow rate of 3 g/h and argon flow rate of 50 l/h.

Fig. 25: Comparison of measured and S/Q simulation results for the carbon monoxide steady-state release rate during isothermal oxidation of Framatome and ESK B_4C pellets for the case of reduced steam flow rate of 3 g/h and argon flow rate of 50 l/h.

Fig. 26: Comparison of measured and S/Q simulation results for the carbon monoxide steady-state release rate during isothermal oxidation of Framatome and ESK B_4C pellets for the case of reduced steam flow rate of 3 g/h and argon flow rate of 50 l/h.

Fig. 27: Comparison of measured and S/Q simulation results for the carbon dioxide release rate during transient temperature oxidation of Framatome B_4C pellet in the test BOX 10406.

Fig. 28: Comparison of measured and S/Q simulation results for the carbon monoxide release rate during transient temperature oxidation of Framatome B_4C pellet in the test BOX 10406.

Fig. 29: Test conditions and measured gas release rate in the test BOX 10607. Isothermal oxidation of Framatome B_4C pellet in argon/steam at 1300 °C.

Fig. 30: S/Q simulation of Framatome B_4C pellet heat up due to B4C oxidation in the test BOX 10607. Comparison of self-consistent and based on measured hydrogen release solutions.

Fig. 31: Comparison of measured and S/Q simulation (with and without consideration of heat release) results for hydrogen release rate during isothermal oxidation of Framatome B_4C pellet in the test BOX 10607.

Fig. 32: Test conditions and measured gas release in the test BOX 10611. Isothermal oxidation of Framatome B_4C pellet in argon/steam at 1400 °C.

Fig. 33: S/Q simulation of Framatome B_4C pellet heat up due to B4C oxidation in the test BOX 10611. Comparison of self-consistent and based on measured hydrogen release solutions.

Fig. 34: Comparison of measured and S/Q simulation (with and without consideration of heat release) results for hydrogen release rate during isothermal oxidation of Framatome B_4C pellet in test BOX 10611.

Fig. 35: Dependence of hydrogen production rate on gas flow velocity at 1000°C and $P_{H_2O} = \text{const.}$

Fig. 36: Dependence of hydrogen production rate on gas flow velocity at 1200°C and $P_{H_2O} = \text{const.}$

Fig. 37: Dependence of hydrogen production rate on gas flow velocity at 1400°C and $P_{H_2O} = \text{const.}$

Fig. 38: Dependence of hydrogen production rate on gas flow velocity with temperature increase from 1200 to 1600°C and $P_{H_2O} = \text{const.}$

Fig. 39: Equilibrium concentrations of dominating gaseous products of the B_4C oxidation reaction on cool-down of the outlet gas mixture, calculated with the IVTAN-Thermo software.

Fig. 40: Corrected average temperature curves. Time interval 3000 – 4000 s.

Fig. 41: Oxide layer thickness axial profile of the corner rod B (withdrawn from the bundle at 3090 s) compared to the calculated one of the central rod at 3090 s.

Fig. 42: Measured oxide layer thickness (averaged over the rods, final status), calculated oxide layer thickness of the central rod at 3564 s (start of bundle flooding) and calculated oxide layer thickness of the central rod (final status). Calculation was performed using corrected temperatures.

Fig. 43: Calculated CO_2, CO and H_2 mass flow rates.

Fig. 44: Calculated B_2O_3, H_3BO_3 and HBO_2 mass flow rates.

Fig. 45: Experimentally measured and calculated C mass flow rate (in CO_2, CO, CH_4).

Fig. 46: Experimentally measured and calculated C mass flow rate (in CO_2, CO, CH_4). Time interval 3300 – 3900 s.

Fig. A-1 Schematic representation the chemical potential gradient across the reaction zones.

1. Introduction

Boron carbide (B_4C) is used as absorber material in Western (BWRs, some PWRs) and Russian (VVER) NPP. During a hypothetical severe accident B_4C can react with steam in the reactor core. The oxidation of B_4C by steam may contribute to degradation of surrounding fuel rods, production of gaseous species (CO, CO_2, CH_4, B_2O_3, boric acids), affecting the fission product chemistry in the primary circuit.

Experimental database on the phenomenon is very limited especially at high temperatures ($T \geq 1000°C$) and in SA codes oversimplified models are used.

To eliminate this deficiency a comprehensive program on B_4C oxidation was launched within the COLOSS Project of the Euratom 5th Framework Programme. In this frame a separate-effects test program on boron carbide oxidation was carried out at Forschungszentrum Karlsruhe using the BOX Rig and thermo-balance facility in a wide range of experimental conditions [1, 2].

On the basis of detailed systematic study of various physico-chemical processes of B_4C oxidation at high temperatures performed in the BOX Rig, a new model for the B_4C oxidation kinetics is developed and presented in the current report. The model self-consistently considers chemical interactions and mass transfer of various species in the multi-component interaction system (solid and liquid interaction layers, gas mixture and their interfaces), and is thoroughly verified against the BOX Rig tests. On the base of the test analysis, new tests are recommended, in order to verify the new model predictions.

The model was implemented in the SVECHA/QUENCH code [3, 4] and applied to simulation of the bundle test QUENCH-07 with the central absorber B_4C rod.

2. Main dependencies of B_4C oxidation kinetics revealed in BOX Rig tests

2.1. Test conduct and observations

The BOX Rig [1] consists of a gas supply system for Ar, H_2 and steam (0-4 mol/h each); a tube furnace (maximum temperature is 1700 °C) with an alumina reaction tube and a quadrupole mass spectrometer (MS). The off-gas tube from the furnace to the MS is heated to about 150 °C to prevent steam condensation. The mass spectrometer allows the quantitative analysis of all gaseous reaction products. In particular, the hydrogen release rate was used in most of the tests as a continuous measure for the reaction kinetics. Besides hydrogen, the main gaseous reaction products of the oxidation of B_4C in water vapour containing atmosphere were carbon monoxide CO and carbon dioxide CO_2. Only small amounts of methane CH_4 were released even during the tests at 800°C, the release rates further decreased with increasing temperature to almost zero above 1000 °C.

Besides the non-condensable gases some masses assigned to boric acids were measured by the mass spectrometer. Boric acids are products of the reaction of B_2O_3 with steam which is believed to play a significant role in the overall oxidation kinetics. Boric acid production was measured only qualitatively due to a missing calibration method and partial condensation in the off-gas system. Nevertheless, it was observed that an enhanced production of orthoboric acid H_3BO_3 was starting at 1100 °C.

Typically test conduct was as follows. The specimens were heated in inert atmosphere (50 l/h at normal conditions, i.e. 0 °C and 1 bar) up to the desired starting temperature for the transient or isothermal oxidation. Then, the steam injection was switched on, usually with a flow rate of 30 g/h. At the end of the oxidation period, the steam flow was switched off and the argon flow increased to 100 l/h, to accelerate the gas exchange from oxidising to inert

atmosphere under which the specimens were cooled. Examples of hydrogen release rate during B_4C isothermal oxidation tests are presented in Fig. 1.

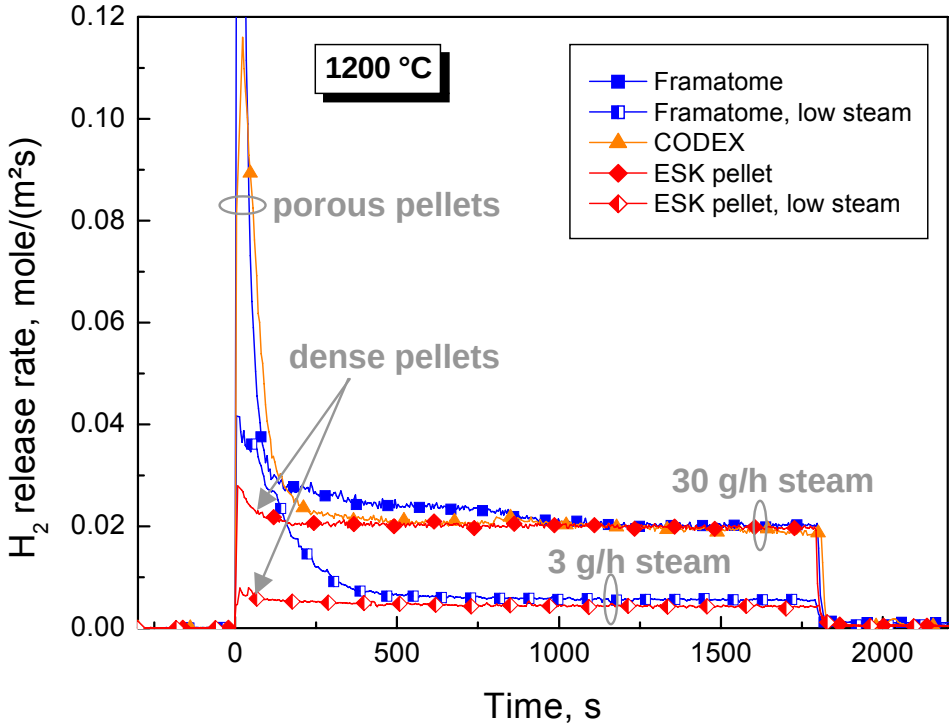

Fig. 1. Hydrogen release during isothermal oxidation of various specimens at 1200°C ([1]).

Three types of B_4C pellets with different porosity were investigated in a wide temperature range. Specimen porosity was ranged from 1 % for ESK pellets to about 30 % for FRAMATOME pellets, as presented in Table 1.

Pellet type	Framatome pellet	CODEX pellet	ESK pellet
Density, g/cm^3	1.8	1.8	2.34
Porosity, %	28.2	19.5	1.3
Pore radii, μm	5-10	1-10	1

Table 1. B_4C specimens used in BOX experiments

The integral mass change of the specimens was additionally measured in all the tests. At 800 °C most of the specimens gained mass due to the formation of boron oxide B_2O_3 remaining in the pores or at the surface of the sample. At higher temperatures the boron oxide increasingly reacts with steam to form volatile boric acids or directly evaporates leading to a mass loss of the specimens. The ESK pellet without open porosity does not gain mass even at the lower temperatures and the powder sample with the highest porosity experiences the highest increase in mass up to 1200 °C. This is probably correlated with the capability to absorb liquid boron oxide.

Fig. 2 illustrates this behaviour in more detail. The B_2O_3 production (green bars) increases with increasing temperature for all specimens, although the boron oxide remaining in the specimen at the end of the test (blue bars) is quite different for the various specimens.

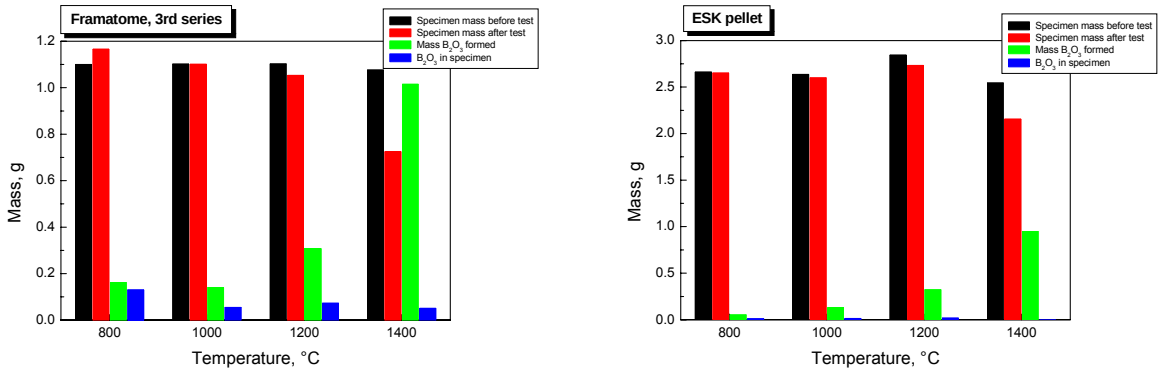

Fig. 2. Pre-test mass (black), post-test mass (red), B_2O_3 formed, recalculated from the hydrogen release data (green), and B_2O_3 remaining in the specimen, calculated as the difference between post-test mass and oxidised B_4C (blue) for the various specimens, in dependence on temperature (from [1]).

Therefore, basing on results obtained in the BOX Rig tests above 1000 °C, the following general conclusions can be derived:

- There are two oxidation stages: initiation phase, with distinct peak of hydrogen production (relatively short at high temperatures) and plateau phase characterised by a constant reaction rate;
- The first peak is caused by oxidation of real pellet surface. The higher porosity corresponds to the higher oxidation rate;
- The plateau phase apparently commences after plugging of open pores and is virtually independent of sample porosity, i.e. is determined by the sample geometrical surface.
- The higher sample porosity corresponds to the higher B_2O_3 content in the sample.

Superposition of two latter suppositions results in conclusion that the oxidation rate of the B_4C sample during the plateau phase is independent of the B_2O_3 content.

Such a behaviour during plateau phase apparently implies that diffusion transport through the liquid oxide layer is not a rate determining process. Indeed, otherwise, owing to increase of the mean (or effective) thickness of the oxide layer for specimens with higher porosity, diffusion barrier for atoms penetration through this layer would also increase in these specimens. In this case oxidation rate during plateau phase should significantly depend on specimen porosity, which was not the case. Moreover, due to possible relocation of liquid oxide layer (detected in some tests) the oxidation rate would be also influenced by the relocation process (leading to decrease of the mean thickness of the oxide barrier), which was not, however, observed in the tests. A more detailed consideration of this problem is presented in Appendix 1.

Hence, the plateau phase may be characterised by interplay between surface chemical kinetics and gas phase mass transfer, manifested by observed oxidation rate dependence on gas flow velocity which is illustrated in the following section.

2.2. Dependence of B_4C oxidation rate on gas dynamic conditions

An example of the oxidation rate dependence on gas dynamic conditions in the BOX Rig tests [1] is demonstrated in Fig. 3. In the plot the results of two tests in similar conditions with the only difference in specimen support are presented. In the first test the specimens were kept in a normal high board alumina boat in the reaction tube. The pellet showed an axially inhomogeneous oxidation due to the inhomogeneous steam flow around the specimen. In the subsequent tests the sample support was changed by sawing off the wall of the alumina boat directed to the steam flow and using an yttria disk as sample support to prevent strong interactions between the B_4C pellets and alumina boat at high temperatures, Fig. 4. As a result of this specimen support improvement, steam access to the pellet enhanced and hydrogen production rate increased more than two times (see Fig. 3).

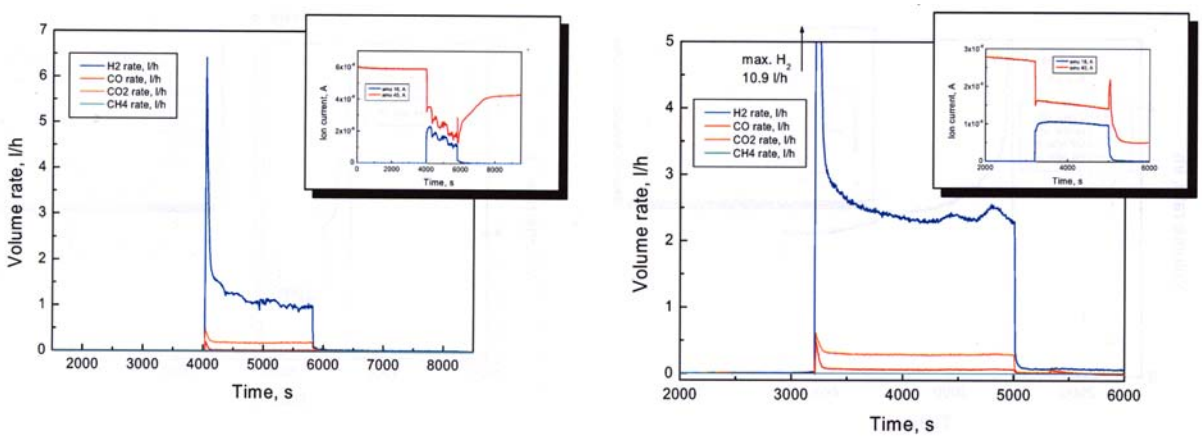

a) deep specimens support (low steam supply)

b) shallow specimens support (high steam supply)

Fig. 3. Oxidation of B_4C specimens at T=1400°C.

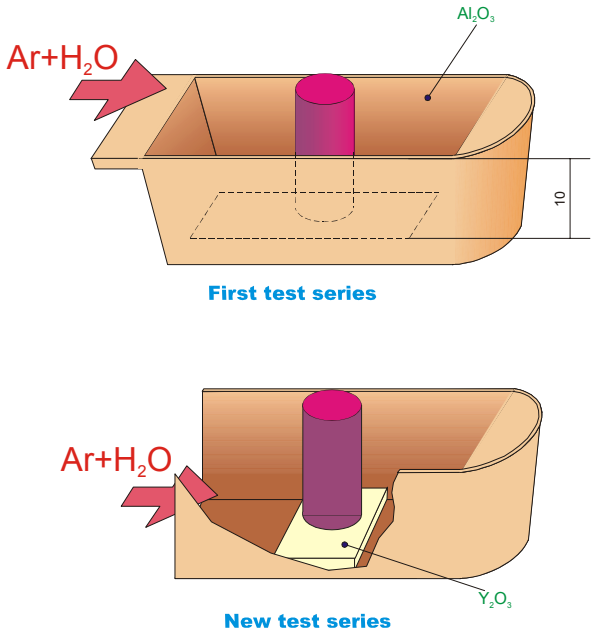

Fig. 4. B_4C specimen support for scoping tests (top) and improved version (bottom).

A similar tendency can be tracked in tests under varying gas atmosphere at 1200 °C (test numbers 10115 and 10126). Conditions and measurement results for two intermediate gas compositions are shown in Table 2. Argon to steam ratios in these mixtures are equal to each other implying equality of steam partial pressures in the bulk of the gas phase. However, these gas mixtures have fairly different gas flow velocities leading to essentially dissimilar oxidation reaction rates, as seen from Table 2.

Test ID	Ar	H_2O	P_{H2O}	Gas velocity	H_2 production
	ln/h	g/h	bar	m/s	mole/m^2s
10115	50	50	0,55	0,2	0,024
10126	30	30	0,55	0,125	0,016

Table 2. Test parameters of experiments on B_4C oxidation in the BOX Rig at 1200°C

The higher flow velocity corresponds to the higher oxidation rate.

Thus, presented in this section observations allow a conclusion that mass transfer in the gas phase has a strong impact on B_4C oxidation rate and should be adequately described in the physical model of the phenomenon.

It is important to note that these observations cannot be explained by simplified models in which dependence of the oxidation rate on gas flow conditions is determined solely by steam partial pressure (which was fixed in these tests).

2.3. Dependence of B_4C oxidation rate on steam partial pressure

For the analysis of the oxidation rate dependence on steam partial pressure, results of two tests under varying gas composition presented in Fig. 5 can be used. These tests were conducted with stepwise changes of inlet atmosphere at 1200 °C.

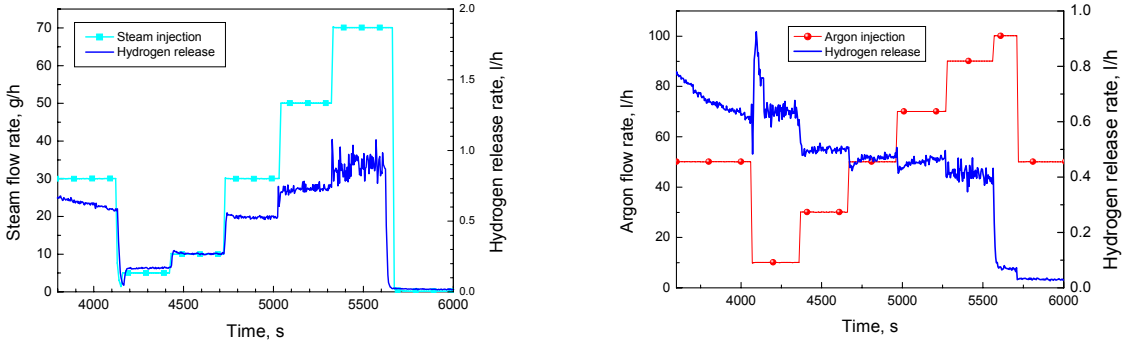

(a) (b)

Fig. 5. Influence of steam (a) and argon (b) flow rate on oxidation kinetics at 1200°C.

Results of these tests along with evaluated steam partial pressures and gas flow velocities are shown in Table 3 and Table 4.

Steam flow rate	Steam partial pressure	Gas flow velocity	Hydrogen release rate
g/h	bar	m/s	mole/m^2s
5	0,11	0,1	0,00564
10	0,2	0,11	0,00889
30	0,43	0,16	0,0176
50	0,55	0,21	0,02404
70	0,63	0,258	0,02956

Table 3. Tests under varying steam production rate (Box 10115)

Argon flow rate	Steam partial pressure	Gas flow velocity	Hydrogen release rate
g/h	bar	m/s	mole/m^2s
10	0,79	0,09	0,021
30	0,55	0,126	0,017
50	0,43	0,16	0,016
70	0,35	0,2	0,015
90	0,3	0,24	0,021

Table 4. Tests under varying argon flow rate (Box 10126)

As can be seen from Tables 3 and 4, in these tests a noticeable change of the gas flow velocity takes place along with the steam partial pressure variation.

In order to separate impact of different factors on B_4C oxidation rate and to evaluate a dependence of the reaction rate solely on steam partial pressure, the data with close flow velocities were selected from Tables 3 and 4 and compiled in Table 5. The selected data are also visualised in Fig. 6.

Steam partial pressure	Gas flow velocity	Hydrogen release rate
bar	m/s	mole/m^2s
0,79	0,09	0,021
0,55	0,126	0,017
0,11	0,1	0,00564
0,2	0,11	0,00889
0,43	0,16	0,0176

Table 5. Summary of test results (Box 10115 and Box 10126)

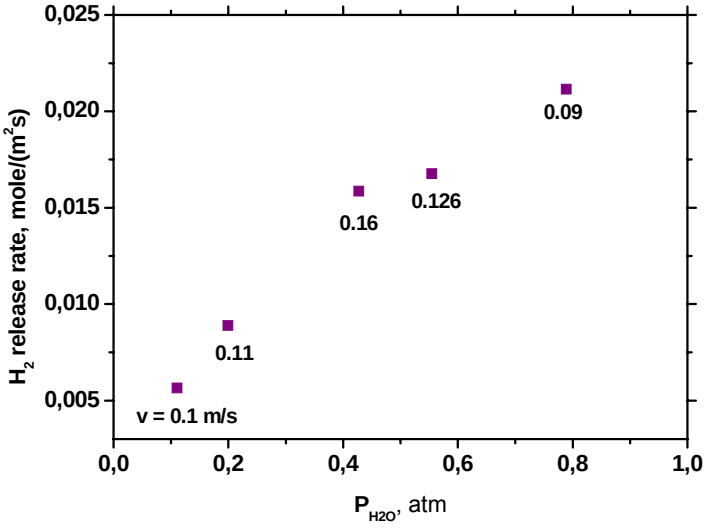

Fig. 6. Dependence of hydrogen release rate on bulk steam partial pressure. Compilation of Box 10115 and Box 10126 test data.

Analysis of these data shows that the dependence of the reaction rate on the steam partial pressure P_{H_2O} is close to linear:

$$\frac{dN_{B_4C}}{dt} = W\left(P_{H_2O}, T\right) = \alpha(T) P_{H_2O}^{a},$$

where the exponent $a \approx 1$.

In the course of model validation (presented in Section 4) against Box Rig tests at various temperatures, the power dependence on steam partial pressure in Eq. (1) was slightly varied, i.e. exponents somewhat different from 1 were tested. Finally it was confirmed that the linear dependence provides the best fit to the complete set of the BOX Rig tests (performed under simultaneously varied steam partial pressure and flow rate).

Additional dependence of the reaction rate on the total gas pressure P_{tot} was revealed in the literature and recently confirmed in the VERDI test program at IRSN [5], which was represented by additional factor in the reaction rate:

$$\frac{dN_{B_4C}}{dt} = W\left(P_{H_2O}, P_{tot}, T\right) = \alpha(T) P_{H_2O}^{a} P_{tot}^{b},$$

with the exponent $b \approx -0.78$, whereas the exponent a was fitted as ≈ 1.18.

However, since the analysed BOX Rig tests were performed under the atmospheric pressure, this dependence on the total gas pressure was not verified in the tests and thus not included in the current model. Nevertheless, taking into account possible applications to the reactor case, both options corresponding to $a \neq 1$ and $b \neq 0$ are reserved in the B_4C oxidation module implemented in the SVECHA/QUENCH (S/Q) code.

Furthermore, it should be noted that the reaction rate is determined by the steam partial pressure near the reaction surface $P_{H_2O}(s)$, whereas the estimated in Table 5 are steam

partial pressures $P_{H_2O}(b)$ in the gas bulk. However, the difference between the two pressures ΔP_{H_2O} under the test conditions is relatively small in comparison with their absolute values, $\Delta P_{H_2O} = P_{H_2O}(s) - P_{H_2O}(b) << P_{H_2O}(s)$, and thus may be neglected within the first order of accuracy. For this reason, the reaction rate can be represented in a more adequate form:

$$\frac{dN_{B_4C}}{dt} = W\left(P_{H_2O}(s), T\right) = \alpha(T) P_{H_2O}(s), \qquad (1)$$

and the bulk values of the steam partial pressure $P_{H_2O}(b)$ from Table 5 can be used in Eq. (1) for analysis of the oxidation rate dependence on the surface partial pressure with a sufficient (first order) accuracy.

On the other hand, in further calculations of the mass transfer in the gas phase (see Section 3.3), the steam flux across the transition boundary layer in the gas phase is directly proportional to the small value ΔP_{H_2O} and thus cannot be neglected within the same (first order) accuracy of the flux calculations.

Such an approximation for Eq. (1) will be avoided in a more detailed analysis of the BOX Rig test results (presented in Section 4.1) with the new B_4C oxidation model implemented in the S/Q code, in which surface chemical kinetics and mass transfer in the gas phase are more adequately coupled and thus the difference between the surface and bulk partial pressures ΔP_{H_2O} in Eq. (1) is more accurately taken into consideration.

2.4. Temperature dependence of B_4C oxidation rate

Preliminary analysis of the test results in the above described approximation of Eq. (1) shows that dependence of the specific reaction rate $\alpha(T) = W(P_{H_2O}, T) / P_{H_2O}$ on temperature presented in Fig. 7 can be searched in the form of the Arrhenius type plot:

$$\alpha(T) = K_1 \exp\left(-E_1/kT\right) + K_2 \exp\left(-E_2/kT\right) \qquad (2)$$

The obtained dependence of oxidation rate on reverse temperature at fixed steam partial pressure is characterised by a non-linear behaviour. This result is distinctly confirmed by more accurate calculations with the S/Q code, see Section 4.1. A plausible reason for deviation from a simple law characterised by one Arrhenius exponent may be connected either with uncontrolled temperature growth due to the oxidation reaction heat generation, or with change of the rate determining process.

The first reason is associated with the test conduct procedure. Hence, according to [1], the specimens were usually heated in inert atmosphere up to the desired starting temperature for isothermal oxidation. Then the steam injection was switched on and oxidation started. However, the oxidation of B_4C by steam is highly exothermic reaction and could induce further temperature escalation. This effect is more pronounced at high temperatures, since the oxidation rate increases with temperature. However, detailed analysis with the S/Q code presented in Section 4.5 shows that this thermal effect is small and can be generally neglected.

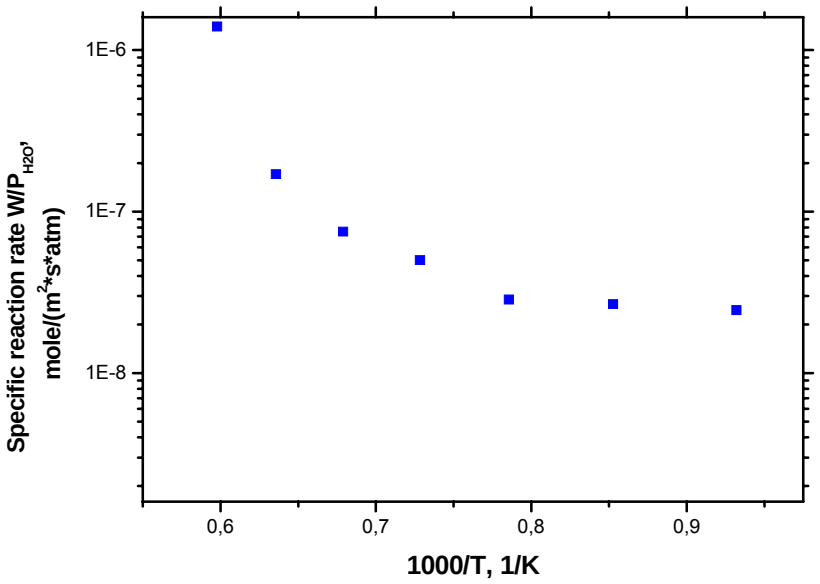

Fig. 7. Calculated specific reaction rate $\alpha(T) = W(P_{H_2O}, T) / P_{H_2O}$ as function of temperature.

The second reason is illustrated in Fig. 8. In this diagram a complex chemical reaction with two parallel processes having different activation energies is considered. Each of two elementary processes has a simple Arrhenius form (dashed lines in Fig. 8), however the total kinetic curve (solid line in Fig. 8) may have a slope similar to one in Fig. 7 obtained as a result of experimental data treatment. A possible reason for such a behaviour will be presented in Section 3.1.

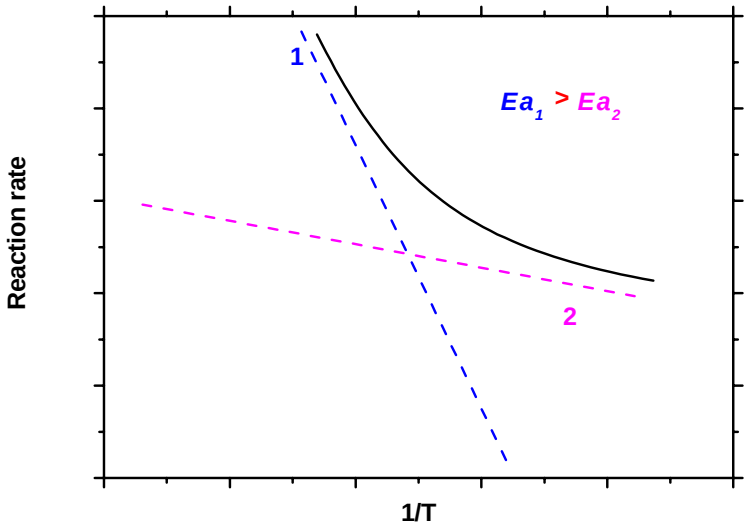

Fig. 8. Schematic representation of total complex reaction rate as function of temperature. Curves 1 and 2 represent two parallel stages.

3. Modelling approach to B_4C oxidation by steam

In the majority of the BOX Rig tests Ar and steam constitute two main components of gas mixture. This mixture of gases is blown through the annular reaction tube (inner diameter: 32 mm, length: 600 mm) where it interacts with B_4C cylindrical specimen placed across the gas flow. Under typical test conditions (argon flow rate ~ 50 l/h at normal conditions, steam flow rate ~ 30 g/h, total pressure ~ 1 atm, Reynolds number ~ 5) the laminar regime of the gas flow in the channel occurs. In this case the gas mass transfer problem can be converted to the problem of the molecular multi-component diffusion through the gas boundary layer near the gas/solid interface.

The model is schematically illustrated in Fig. 9, where the B_4C cylindrical specimen axis is oriented along the gas flow, similarly to orientation of the absorber fuel rods in the reactor flow channel. In the geometry of the BOX Rig tests the specimen is placed across the steam/argon gas as shown in Fig. 4. This difference in the B_4C specimen orientation will be formally taken into account when a correlation for the mass transfer coefficient in the gas phase will be chosen, see Section 3.5.

Water molecules are transported from the bulk of the gas phase to the specimen surface where chemical reactions take place and oxidation products are generated which in its turn are transported back into the bulk of the gas flow.

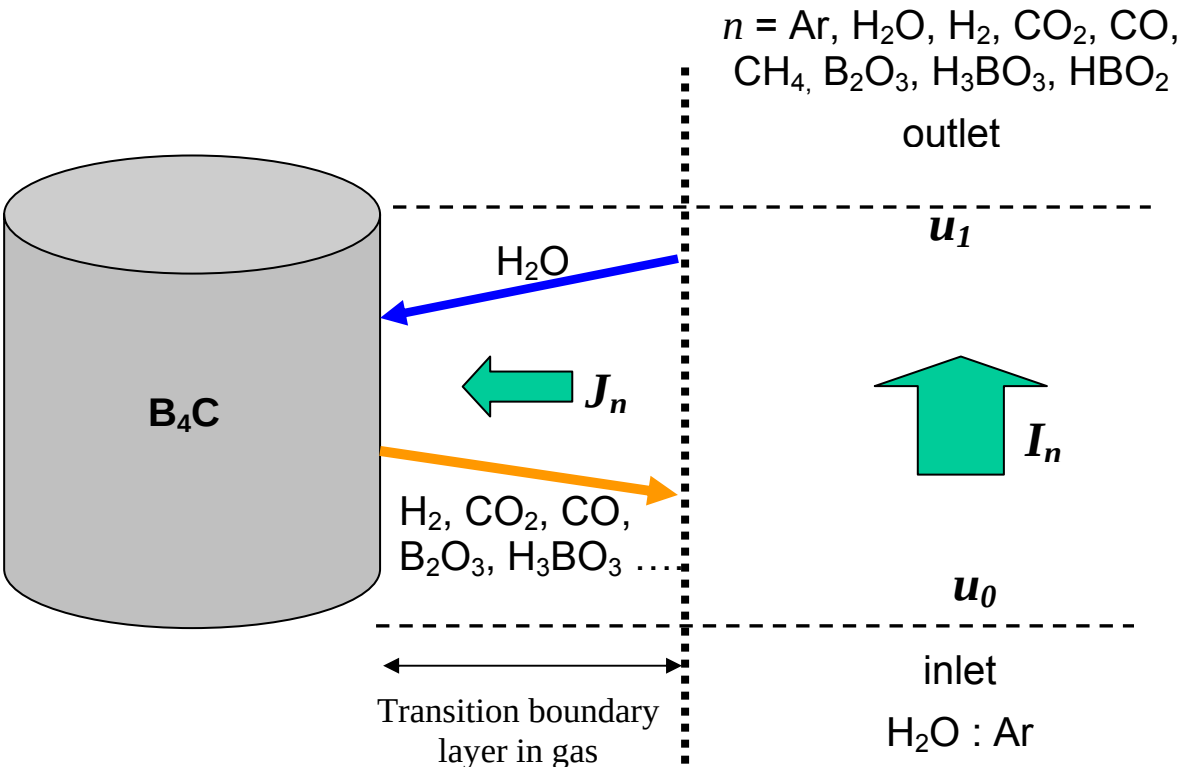

Fig. 9. Schematic representation of the model.

3.1. Main chemical processes at the reaction interface

The main registered in the experiments gaseous reaction products are hydrogen, carbon monoxide, carbon dioxide and methane formed along with the liquid boron oxide in the following reactions:

$$B_4C(s) + 7H_2O(g) = 2B_2O_3(l) + CO(g) + 7H_2(g), \quad (3)$$

$$B_4C(s) + 8H_2O(g) = 2B_2O_3(l) + CO_2(g) + 8H_2(g), \quad (4)$$

$$B_4C(s) + 6H_2O(g) = 2B_2O_3(l) + CH_4(g) + 4H_2(g). \quad (5)$$

At high temperatures the liquid boron oxide directly evaporates or reacts with steam to form volatile boric acids leading to a mass loss of the specimens in the reactions:

$$B_2O_3(l) = B_2O_3(g), \quad (6)$$

$$B_2O_3(l) + 3\,H_2O(g) = 2\,H_3BO_3(g) \text{ (orthoboric acid)}, \quad (7)$$

$$B_2O_3(l) + H_2O(g) = 2\,HBO_2(g) \text{ (metaboric acid)}. \quad (8)$$

Superposition of Eqs. (3)-(5) and Eqs. (6)-(8) results in altogether $3\times3 = 9$ chemical reactions of B_4C with steam resulting in formation of gaseous products. Until these reactions are considered as equilibrium, only five of them are independent, i.e. each of the nine reactions can be obtained as a linear combination of the reactions from the independent set. It is most convenient to choose the following five reactions as the independent set:

$$B_4C(s) + 8\,H_2O(g) = 2\,B_2O_3(g) + CO_2(g) + 8\,H_2(g), \quad (9)$$

$$B_2O_3(g) + 3\,H_2O(g) = 2\,H_3BO_3(g), \quad (10)$$

$$B_2O_3(g) + H_2O(g) = 2\,HBO_2(g), \quad (11)$$

$$CO(g) + H_2O(g) = CO_2(g) + H_2(g), \quad (12)$$

$$CH_4(g) + H_2O(g) = CO(g) + 3H_2(g), \quad (13)$$

whence linear superposition of Eq. (9) with 4 gaseous reactions Eqs. (10)-(13) allows reproduction of all possible routes of B_4C transformation into the gaseous products in the course of its interaction with steam.

When chemical interactions become rate determining step, some of the chemical reactions cannot be anymore considered as equilibrium. It is most natural to assume that the relatively quick gas reactions Eqs. (10)-(13) remain equilibrium, whereas one of the inter-phase reactions, Eq. (9) or its any other superposition with Eqs. (10)-(13), becomes non-equilibrium:

$$B_4C(s) + 14\,H_2O(g) \rightarrow 4\,H_3BO_3(g) + CO_2(g) + 8\,H_2(g), \quad (14)$$

or

$$B_4C(s) + 8\,H_2O(g) \rightarrow 2\,B_2O_3(g) + CO_2(g) + 8\,H_2(g), \quad (14a)$$

or ...

In various temperature intervals, different non-equilibrium reactions, Eqs. (14), (14a),…, can be rate determining step. In this case the reaction rate constant has to be superposition of various Arrhenius exponents related to the corresponding chemical reactions:

$$\alpha(T) = K_1 \exp\left(-E_1/kT\right) + K_2 \exp\left(-E_2/kT\right) + \ldots, \quad (15)$$

this is in agreement with the test analysis presented in Section 2.4.

Furthermore, it might be assumed that the first activation energy E_1 is determined by formation of the gaseous boric acids (in reaction of liquid B_2O_3 with water molecules, Eq. (7), which is a constituent step of Eq. (14)), whereas the second activation energy E_2 is determined by direct evaporation of B_2O_3 (in reaction Eq. (6), which is a constituent step of Eq. (14a)). As will be shown in Section 4, this assumption is in a qualitative agreement with conclusions from another series of the Thermo-Gravimetric (TG) tests, performed at Forschungszentrum Karlsruhe [2]. On the other hand, this assumption generally does not contradict to extremely small amounts of gaseous B_2O_3 detected in the BOX Rig tests, owing

to quick conversion of this gaseous product into boric acids in the gas mixture, Eq. (10) and (11).

Therefore, Eq. (1) along with Eq. (15) determines the reaction rate equation for the non-equilibrium chemical processes on the reaction surface. Alternatively, the equilibrium gas reactions Eqs. (10)-(13) can be characterized by a system of the corresponding mass action laws:

$$p^3_{H_2O}(s)p_{B_2O_3}(s) = C_1 p^2_{H_3BO_3}(s), \tag{16}$$

$$p_{H_2O}(s)p_{B_2O_3}(s) = C_2 p^2_{HBO_2}(s). \tag{17}$$

$$p_{CO}(s)p_{H_2O}(s) = C_3 p_{CO_2}(s)p_{H_2}(s), \tag{18}$$

$$p_{CH_4}(s)p_{H_2O}(s) = C_4 p_{CO}(s)p^3_{H_2}(s), \tag{19}$$

with the partial pressures normalized by the total pressure in the gas mixture P_{tot}, $p_n = P_n / P_{tot}$.

It is important to note that as soon as the first reaction from the independent set, Eq. (9), is assumed to be non-equilibrium, the corresponding mass action law is not anymore valid, and therefore, Eq. (1) is used instead. Hence, a crucial mistake would be simultaneous use of Eq. (1) and the mass action law for the same chemical reaction Eq. (9).

The identical set of equilibrium gaseous reactions, Eqs. (10)-(13), is valid in the bulk of the gas flow. Therefore, the corresponding set of the mass action laws takes the form:

$$p^3_{H_2O}(b)p_{B_2O_3}(b) = C_1 p^2_{H_3BO_3}(b), \tag{20}$$

$$p_{H_2O}(b)p_{B_2O_3}(b) = C_2 p^2_{HBO_2}(b), \tag{21}$$

$$p_{CO}(b)p_{H_2O}(b) = C_3 p_{CO_2}(b)p_{H_2}(b), \tag{22}$$

$$p_{CH_4}(b)p_{H_2O}(b) = C_4 p_{CO}(b)p^3_{H_2}(b), \tag{23}$$

with the same equilibrium reaction constants as in Eqs. (16)-(19), which are related to the Gibbs energies for the reaction products formation:

$$RT\ln C_1 = 2G^0_{H_3BO_3(g)} - G^0_{B_2O_3(g)} - 3G^0_{H_2O(g)}, \tag{24}$$

$$RT\ln C_2 = 2G^0_{HBO_2(g)} - G^0_{B_2O_3(g)} - G^0_{H_2O(g)}, \tag{25}$$

$$RT\ln C_3 = G^0_{CO_2(g)} + G^0_{H_2(g)} - G^0_{CO(g)} - G^0_{H_2O(g)}, \tag{26}$$

$$RT\ln C_4 = G^0_{CO(g)} + 3G^0_{H_2(g)} - G^0_{CH_4(g)} - G^0_{H_2O(g)}. \tag{27}$$

These Gibbs energies can be calculated using, e.g., the IVTAN-Thermo software [6].

The normalized partial pressures entering Eqs. (16)-(19) and Eqs. (20)-(23), obey the total pressure conservation law near the reaction surface:

$$\sum_n p_n(s) = \sum_n P_n(s)/P_{tot} = 1, \tag{28}$$

and in the bulk of the gas flow:

$$\sum_n p_n(b) = \sum_n P_n(b)/P_{tot} = 1, \tag{29}$$

where n = Ar, H_2O, H_2, CO_2, CO, CH_4, B_2O_3, H_3BO_3, HBO_2.

3.2. Flux matches at the B_4C/gas interface and in the gas bulk

Flux matching conditions on the B_4C surface for the gaseous species Ar, H_2O, H_2, CO_2, CO, CH_4, B_2O_3, H_3BO_3, HBO_2 represent conservation laws on the surface for the following elements:

O:

$$J_{H_2O} + 2J_{CO_2} + J_{CO} + 3J_{B_2O_3} + 3J_{H_3BO_3} + 2J_{HBO_2} = 0, \quad (30)$$

H:

$$2J_{H_2O} + 2J_{H_2} + 3J_{H_3BO_3} + J_{HBO_2} + 4J_{CH_4} = 0, \quad (31)$$

C:

$$J_{CO_2} + J_{CO} + J_{CH_4} = \frac{dN_{B_4C}}{dt}, \quad (32)$$

B:

$$2J_{B_2O_3} + J_{H_3BO_3} + J_{HBO_2} = 4\frac{dN_{B_4C}}{dt}, \quad (33)$$

Ar:

$$J_{Ar} = 0, \quad (34)$$

where J_n are densities of the molar fluxes in the gas boundary layer near the interface, $\frac{dN_{B_4C}}{dt}$ is the number of B_4C moles oxidised per second and per unit square that was defined as the reaction rate in Eq. (1).

In the simplest approximation of small variation in the axial direction of the gas composition (in comparison with the inlet composition of the Ar/H_2O mixture) in Fig. 9, which can be well grounded for relatively short specimens typical for the BOX Rig tests, the conservation laws for the above presented elements can be represented in the form of flux matches in the gas bulk:

O:

$$I_{H_2O} + 2I_{CO_2} + I_{CO} + 3I_{B_2O_3} + 3I_{H_3BO_3} + 2I_{HBO_2} = I^{(0)}_{H_2O}, \quad (35)$$

H:

$$2I_{H_2O} + 2I_{H_2} + 3I_{H_3BO_3} + I_{HBO_2} + 4I_{CH_4} = 2I^{(0)}_{H_2O}, \quad (36)$$

C:

$$\left(I_{CO_2} + I_{CO} + I_{CH_4}\right)\frac{S_{outlet}}{S_{surf}} = J_{CO_2} + J_{CO} + J_{CH_4} = \frac{dN_{B_4C}}{dt}, \quad (37)$$

B:

$$\left(2I_{B_2O_3} + I_{H_3BO_3} + I_{HBO_2}\right)\frac{S_{outlet}}{S_{surf}} = 2J_{B_2O_3} + J_{H_3BO_3} + J_{HBO_2} = 4\frac{dN_{B_4C}}{dt}, \quad (38)$$

Ar:

$$I_{Ar}^{(0)} = I_{Ar}\,, \tag{39}$$

where $I_n = u_1 P_n(b)/RT$ are outlet axial fluxes of the gaseous components, n = Ar, H_2O, H_2, CO_2, CO, CH_4, B_2O_3, H_3BO_3, HBO_2; S_{surf} is the sample surface area; S_{outlet} is the outlet gas channel cross section area;

$I_{Ar}^{(0)} = u_0 P_{Ar}^{(0)}(b)/RT$ and $I_{H_2O}^{(0)} = u_0 P_{H_2O}^{(0)}(b)/RT = u_0\left(P_{tot} - P_{Ar}^{(0)}(b)\right)/RT$ are inlet axial fluxes of Ar and H_2O; R is the universal gas constant, and $u_{0(1)}$ is inlet (outlet) gas velocity, see Fig. 9.

For the more prototypic reactor geometry where axial variation of the gas composition becomes substantial, a more precise procedure of axial meshing and corresponding gas conservation equations will be presented in Section 3.5.

3.3. Diffusion fluxes in the gas boundary layer

In the case typical for the BOX Rig tests when there are two major components Ar (n = 1) and H_2O (n = 2) in the gas mixture, the molar diffusion fluxes in the gas boundary layer near the interface J_n can be approximated for the dominating pair of the gases as:

$$J_1 = K_1\left(X_2\Delta P_1 - X_1\Delta P_2\right) - X_1\sum_{n=3}^{9} K_n\Delta P_n + K_{conv}P_1(s), \tag{40}$$

$$J_2 = K_1\left(X_1\Delta P_2 - X_2\Delta P_1\right) - X_2\sum_{n=3}^{9} K_n\Delta P_n + K_{conv}P_2(s), \tag{41}$$

and for the other low-concentration components as:

$$J_n = K_n\Delta P_n + K_{conv}P_n(s), \quad n = 3,\ldots 9\,, \tag{42}$$

where $\Delta P_i = P_i(s) - P_i(b)$, $X_1 = \dfrac{P_1(s)}{P_1(s)+P_2(s)}$, $X_2 = \dfrac{P_2(s)}{P_1(s)+P_2(s)}$,

and $v_{conv} = K_{conv}/RT$ is the gas net velocity affording conservation of the total gas pressure P_{tot} across the boundary layer and determining the total molar flux

$$\sum_{n=1}^{9} J_n = K_{conv}P_{tot}\,.$$

Diffusion mass transfer coefficients are represented in the standard form:

$$K_i = \frac{1}{RT}\cdot\frac{D_i}{d}\mathrm{Sh}_i\,, \tag{43}$$

where d is the sample diameter, Sh is the Sherwood number. For the case of the forced convection flow across a circular cylinder the Sherwood number can be approximated by a correlation [7]:

$$\mathrm{Sh}_i = A\cdot\mathrm{Re}^m\,\mathrm{Sc}_i^{\,0.37}\varepsilon_q\,, \tag{44}$$

where Sc_i is the Schmidt number, $\mathrm{Sc}_i = \mu/(\rho D_i)$ μ and ρ are viscosity and density of gas mixture, respectively;

$$\varepsilon_q = \left[1 - \left(\frac{d}{d_h}\right)^2\right]^m$$

is the geometrical correction factor, d_h is the flow channel hydraulic diameter.

Parameters A and m of the relation (44) are presented in Table 6 for Reynolds numbers in the range of interest of the BOX tests.

Re	A	m
0.05 ÷ 2	0.640	0.305
2 ÷ 4	0.556	0.41
4 ÷ 500	0.381	0.47

Table 6. Parameters A and m for different Reynolds numbers.

3.3.1. Viscosity of gas mixture

Viscosity of the binary gas mixture is calculated by Wilke's formula [8]:

$$\mu_{1,2}^0 = \frac{\mu_1^0}{1 + \frac{X_2}{X_1}\Phi_{1,2}} + \frac{\mu_2^0}{1 + \frac{X_1}{X_2}\Phi_{2,1}}, \tag{45}$$

where

$$\Phi_{1,2} = \frac{\left[1 + \sqrt{\frac{\mu_1^0}{\mu_2^0}}\left(\frac{M_2}{M_1}\right)^{0.25}\right]^2}{2\sqrt{2}\left(1 + \frac{M_1}{M_2}\right)^{0.5}}, \qquad \Phi_{2,1} = \Phi_{2,1}\frac{\mu_2^0}{\mu_1^0}\frac{M_1}{M_2},$$

μ^0_1, M_1 and μ^0_2, M_2 are viscosity, molar weight of the first and the second main component of gas mixture under normal conditions. Viscosity at a given temperature and pressure is determined from Eq. (17) and correlation [9]:

$$\mu^T = \mu^0 \frac{273 + C}{T + C}\left(\frac{T}{273}\right)^{\frac{3}{2}}. \tag{46}$$

The parameters introduced in Eq. (46) are specified in Table 7.

Gas	μ^0, N·s/m^2	Saterland's constant, C
Ar	$2.114 \cdot 10^{-5}$	142
H_2O	$0.861 \cdot 10^{-5}$	650

Table 7. Standard viscosity and Saterland's constant for steam and argon.

3.3.2. Gas diffusion coefficients in gas mixture

Gas diffusion coefficient $D_{n,AB}$ of small admixture n in mixture of two major gases (A+B) is determined by the interdiffusion coefficients in corresponding binary mixtures:

$$\frac{P_{tot} - P_n}{D_{n,AB}} = \frac{P_A}{D_{n,A}} + \frac{P_B}{D_{n,B}}, \qquad (47)$$

where $D_{n,A}$ and $D_{n,B}$ are the interdiffusion coefficients of binary mixtures (n, A) and (n, B), respectively; P_A and P_B are the partial pressures of the main components A and B.

As shown in numerous investigations, results of experimental measurements of the interdiffusion coefficients are well approximated in the form:

$$D = \frac{D_0}{P_{tot}} \cdot (T/273)^a, \quad [P_{tot}]=\text{atm}, \qquad (48)$$

where T is the temperature in K. The constants D_0 and a for different mixtures taken from [9, 10] are presented in Table 8.

Mixture	D_0 (cm^2/s)	a
H_2 – Ar	0.75	1.89
H_2 – H_2O	0.734	1.820
CO_2 – Ar	0.177	1.65
CO_2 – H_2O	0.146	1.84

Table 8. Parameters of binary diffusion for gas mixtures.

The other required diffusion coefficients are calculated by using an empirical correlation proposed in [11]:

$$D_{n,A} = 2.79\times10^{-3} \frac{T^{1.622}}{P_{tot}\left(V_n^{1/3} + V_A^{1/3}\right)^2} \sqrt{\frac{1}{M_n} + \frac{1}{M_A}} \quad (\text{cm}^2/\text{s}), \qquad (49)$$

where M_n – molecular weight, g/mole; V_n – critical molar volume, cm^3/mole.

The latter is defined as the ratio between the molar mass and the density of the species in the condensed state under normal conditions. Values of critical volumes from [10, 11] are presented in Table 9.

Species	H_2O	Ar	H_3BO_3
V_i, cm^3/mol	56.3	75.2	43

Table 9. Values of critical volumes.

3.4. Complete set of equations

The above presented equations present a complete set which can be applied to simulation of the B_4C oxidation kinetics, observed for example, in the BOX Rig tests. Indeed, there were introduced in the model altogether 21 unknown variables,

11 on the surface:

$$9[P_n(s)]+1[K_{conv}]+1[\dot{N}_{B_4C}] = 11\ ,$$

and 10 in the bulk:

$$9[P_n(b)]+1[u_1] = 10.$$

These unknown variables enter in 21 equations,

11 on the surface:

> 4 [mass action laws, Eqs. (16) - (19)] + 1 [oxidation rate, Eq. (1)] + 5 [flux matches, Eq. (30)-(34)] + 1 [pressure conservation, Eq. (28)] = 11,

and 10 in the bulk:

> 4 [mass action laws, Eqs. (20)-(23)] + 5 [flux matches, Eq. (35)-(39)] + 1 [pressure conservation, Eq. (29)] = 10.

Solution of this set of 21 independent equations allows calculation of the 21 unknown variables, which determine the B_4C oxidation kinetics measured in the BOX Rig tests.

This set of equations can be further extended, if necessary, to consideration of new (minor) reaction products in a self-consistent manner: for each new gas component (characterised by two unknown variables: surface and bulk pressures) two additional equations (mass action laws in the bulk and on the surface) along with additional terms in the same set of flux matches, will be supplemented.

For instance, an additional consideration of the trimer of metaboric acid $H_3B_3O_6$ among the oxidation products requires implementation into the independent set of chemical reactions, Eqs. (9)-(13), of an additional equilibrium gaseous reaction:

$$3\ H_3BO_3(g) = H_3B_3O_6(g) + 3\ H_2O(g),$$

and implementation of the corresponding 2 mass action law equations into the systems of Eqs. (16)-(19) and Eqs. (20)-(23) for the normalized partial pressure $p_{H_3B_3O_6} = P_{H_3B_3O_6}/P_{tot}$ near the surface and in the gas bulk:

$$p^3_{H_3BO_3}(s) = C_5\, p_{H_3B_3O_6}(s)\, p^3_{H_2O}(s),$$

$$p^3_{H_3BO_3}(b) = C_5\, p_{H_3B_3O_6}(b)\, p^3_{H_2O}(b),$$

and introduction of new terms $J_{H_3B_3O_6}$ and $I_{H_3B_3O_6}$ in the flux matching Eqs. (30), (31), (33) and Eqs. (35), (36), (38) for conservation of O, H and B, respectively; for instance, Eq. (38) for B takes in this case the form:

$$\left(2I_{B_2O_3} + I_{H_3BO_3} + I_{HBO_2} + 3I_{H_3B_3O_6}\right)\frac{S_{outlet}}{S_{surf}} = 2J_{B_2O_3} + J_{H_3BO_3} + J_{HBO_2} + 3J_{H_3B_3O_6} = 4\frac{dN_{B_4C}}{dt}. \quad (38')$$

Therefore, an extended set of 23 unknown variables will be uniquely calculated from the new system of 23 independent equations.

Consideration of acid $H_3B_3O_6$ might be important at temperatures below 1400 K, according to the thermo-chemical equilibrium calculations with the IVTAN-Thermo software [6], see Section 5.2.

Additional consideration of some minor gaseous reaction products such as OH, H, BO_2, etc., which might be important at high temperatures above 1900 K, can be implemented in the new model in a similar manner.

3.5. Model implementation in the SVECHA/QUENCH code

The computer SVECHA/QUENCH (S/Q) code was developed in the Nuclear Safety Institute (IBRAE) of Russian Academy of Sciences for the detailed modelling of reflooding phenomena observed in the single-rod QUENCH rig tests (Forschungszentrum Karlsruhe), in close cooperation with German experimentalists [3, 4]. Within the framework of the S/Q code the main physical phenomena occurring during degradation of fuel rods are considered: cladding oxidation, cladding mechanical deformation, hydrogen uptake and release, heat conduction inside the fuel rod, heat and mass exchange in the surrounding two-phase media. For the adequate description of the profound mutual influence of the above phenomena the self-consistent coupling of the Oxidation, Mechanical Deformation, Hydrogen Absorption, Heat Conduction and Thermal-Hydraulic models in the SVECHA/QUENCH code was performed.

In order to apply the B_4C oxidation model to the prototypic reactor geometry, in which considerable variation along the absorber rod of the gas composition can take place owing to the chemical interactions, the model was implemented in the S/Q code. This allows also more detailed and accurate analysis of the results obtained in the BOX Rig tests, for instance, investigation of the heat release owing to B_4C oxidation by steam and its possible influence on the oxidation kinetics owing to temperature escalation on the reaction surface.

For this purpose meshing in the axial direction is introduced as schematically shown in Fig. 10. Correspondingly, the conservation laws for molar concentrations C_k of the implicated elements C, B, O, H and Ar in the gas bulk take the form:

$$\frac{\partial C_k}{\partial t} = -div\left(\tilde{I}_k\right) + \tilde{J}_k, \qquad k = \text{H, O, B, C, Ar,} \tag{50}$$

where

$$\tilde{I}, \tilde{J}_C \equiv I, J_{CO_2} + I, J_{CO} + I, J_{CH_4},$$

$$\tilde{I}, \tilde{J}_B \equiv 2I, J_{B_2O_3} + I, J_{H_3BO_3} + I, J_{HBO_2},$$

$$\tilde{I}, \tilde{J}_O \equiv I, J_{H_2O} + 2I, J_{CO_2} + I, J_{CO} + 3I, J_{B_2O_3} + 3I, J_{H_3BO_3} + 2I, J_{HBO_2},$$

$$\tilde{I}, \tilde{J}_H \equiv 2I, J_{H_2O} + 2I, J_{H_2} + 4I, J_{CH_4} + 3I, J_{H_3BO_3} + I, J_{HBO_2},$$

$$\tilde{I}, \tilde{J}_{Ar} \equiv I, J_{Ar}$$

The axial fluxes in the channel are defined in each mesh *i* with the volume ΔV_i as

$$\tilde{I}_k^{(i)} = C_k^{(i)} u^{(i)}, \quad k = \text{C, B, O, H, Ar,}$$

along with the local gas velocities $u^{(i)}$ and molar concentrations $C_k^{(i)}$, which obey the relationships:

$$C_C^{(i)} = C_{CO_2}^{(i)} + C_{CO}^{(i)} + C_{CH_4}^{(i)} = \left(P_{CO_2}^{(i)}(b) + P_{CO}^{(i)}(b) + P_{CH_4}^{(i)}(b)\right) \Big/ RT,$$

$$C_B^{(i)} = \left(2P_{B_2O_3}^{(i)}(b) + P_{H_3BO_3}^{(i)}(b) + P_{HBO_2}^{(i)}(b)\right) \Big/ RT,$$

$$C_O^{(i)} = \left(P_{H_2O}^{(i)}(b) + 2P_{CO_2}^{(i)}(b) + P_{CO}^{(i)}(b) + 3P_{B_2O_3}^{(i)}(b) + 3P_{H_3BO_3}^{(i)}(b) + 2P_{HBO_2}^{(i)}(b)\right) \Big/ RT,$$

$$C_H^{(i)} = \left(2P_{H_2O}^{(i)}(b) + 2P_{H_2}^{(i)}(b) + 4P_{CH_4}^{(i)}(b) + 3P_{H_3BO_3}^{(i)}(b) + P_{HBO_2}^{(i)}(b)\right) \Big/ RT,$$

$$C_{Ar}^{(i)} = P_{Ar}^{(i)}(b)/RT$$

The radial fluxes additionally obey the mass conservation laws of the elements on the reaction surface:

$$\tilde{J}_B^{(i)} = 4\tilde{J}_C^{(i)} = 4\dot{N}_{B_4C}^{(i)} \frac{S_{surf}^{(i)}}{\Delta V_i} = 4\alpha(T) P_{H_2O}^{(i)}(s) \frac{S_{surf}^{(i)}}{\Delta V_i}, \quad (51)$$

$$\tilde{J}_H^{(i)} = \tilde{J}_O^{(i)} = \tilde{J}_{Ar}^{(i)} = 0. \quad (52)$$

These equations along with the total pressure conservation:

$$\sum_{n=1}^{9} P_n^{(i)}(b) = \sum_{n=1}^{9} P_n^{(i)}(s) = P_{\text{tot}}, \quad (53)$$

n = Ar, H_2O, H_2, CO_2, CO, CH_4, B_2O_3, H_3BO_3, HBO_2,

and the mass action laws Eqs. (16)-(19) and Eqs. (20)-(23) applied to each axial mesh *i*, assemble a complete system of equations for calculation of the oxidation kinetics by the S/Q code.

For the geometry of the absorber rod in the reactor flow channel and stabilized laminar flow conditions, the Sherwood number in the gas phase instead of Eq. (44) is constant [7]:

$$\text{Sh} = 3.66. \quad (54)$$

For turbulent flow the following correlation is applied:

$$\text{Sh}_i = 0.023 \cdot \text{Re}^{0.8} \, \text{Sc}_i^{\,0.4}. \quad (55)$$

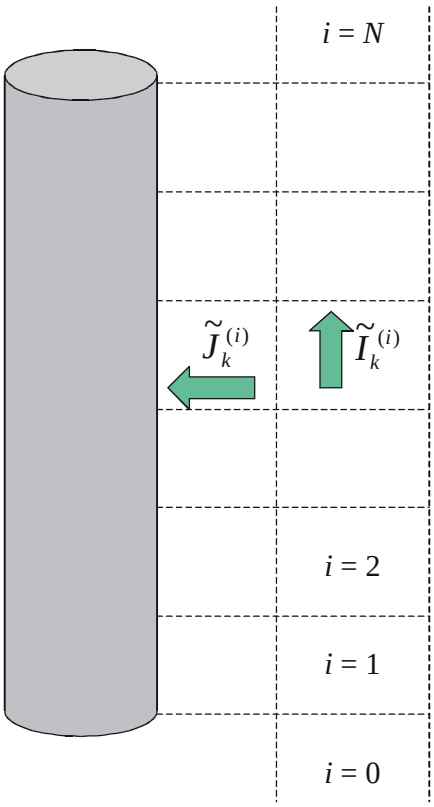

Fig. 10. Schematic representation of the model implemented in the S/Q code.

4. Verification of B_4C oxidation model against BOX Rig tests

4.1. Fitting of model parameters against isothermal tests

All isothermal tests from the BOX Rig test series with reliable gas release measurement were selected for the analysis. The tests with duration 30 minutes at temperatures between 800 and 1400 °C under steam flow rate of 30 g/h and argon flow rate of 50 l/h and, hence, at the same bulk steam partial pressure and gas flow velocity, are presented in Table 10. This selection allows direct comparison of various tests with each other.

Test ID	Temperature	Argon	Steam	Specimen	H_2 release rate
	° C	ln/h	g/h		mole/m^2s
10405	800	50	30	Framatome	0.00768
10907	800	50	30	CODEX	0.00560
10927	800	50	30	ESK pellet	0.00360
10511	900	50	30	Framatome	0.00800
10219	1000	50	30	Framatome	0.01040
10514	1000	50	30	Framatome	0.00880
10910	1000	50	30	CODEX	0.00880
11001	1000	50	30	ESK pellet	0.00800
10605a	1100	50	30	Framatome	0.01440
10911	1200	50	30	CODEX	0.02000
11002	1200	50	30	ESK pellet	0.02000
10607	1300	50	30	Framatome	0.03680
10611	1400	50	30	Framatome	0.07920
10912	1400	50	30	CODEX	0.06080
11004	1400	50	30	ESK pellet	0.05680

Table 10. Test conditions and results of isothermal tests on B_4C oxidation in the BOX Rig. Steam flow rate of 30 g/h and argon flow rate of 50 l/h

The hydrogen release rates in Table 10 were obtained by recalculation of the measured B_4C oxidation rates with the help of the rule [1]:

$$[H_2 \text{ release rate in mole}/(m^2 s)] = [B_4C \text{ consumption rate in mole}/(m^2 s)] \times 8. \quad (56)$$

It should be noted that only tests with B_4C pellets were selected whereas the tests with B_4C powder (as well as the first scoping tests performed with a normal alumina boat, see Section 2.2) were not taken into consideration.

The hydrogen release rates during the steady-state (or plateau) stage for all isothermal tests presented in Table 10 are plotted in the form of the Arrhenius type diagram in Fig. 11.

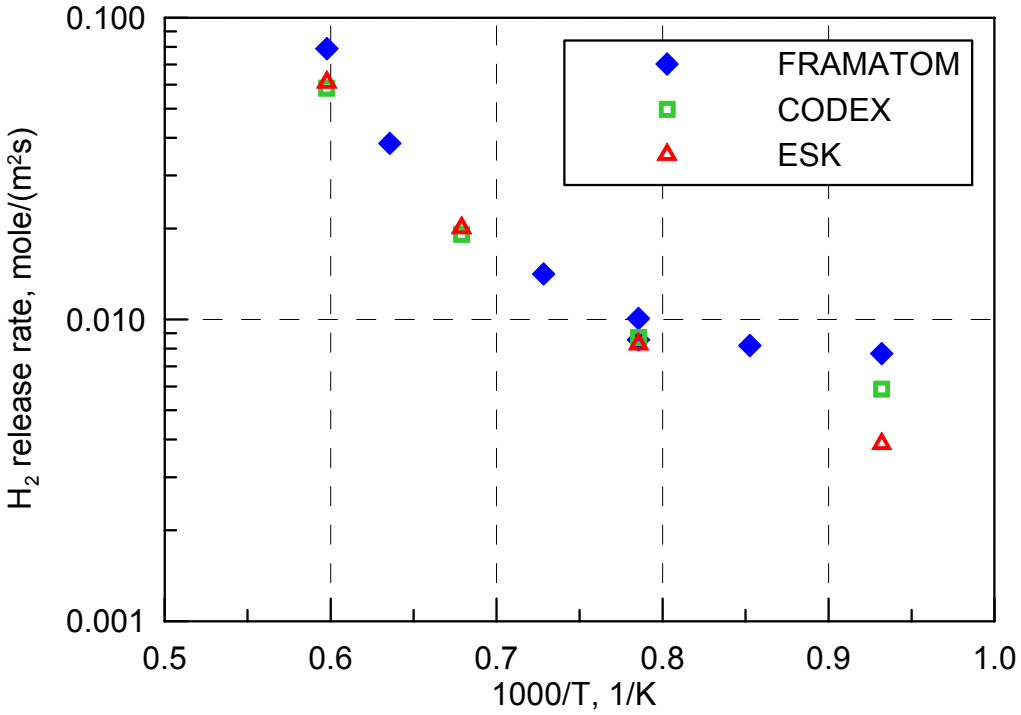

Fig. 11. Measured hydrogen release rate during isothermal oxidation of different type of B_4C pellet for the case of steam flow rate of 30 g/h and argon flow rate of 50 l/h.

From Fig. 11 one can distinguish the following main features:

- The hydrogen release rates for different samples virtually coincide, however, a slight deviation between the rates can be detected at low and high temperatures;
- For all types of the pellets the hydrogen release rate as a function of the reverse absolute temperature deviates from the simple Arrhenius law (with one exponent).

As discussed in Section 2.4, the deviation of the specific reaction rate $\alpha(T)$ from a simple law characterised by one Arrhenius exponent may be explained by a complex chemical reaction with two parallel stages having different activation energies. Each of the two elementary stages has a simple Arrhenius form, whereas the total kinetic curve is a superposition of these two Arrhenius laws, Eq. (2).

A similar conclusion was done in [2], where Thermo-Gravimetric (TG) examinations on the oxidation of B_4C were carried out. In these tests the sensitive balance system was used to measure mass change of B_4C or B_2O_3 specimens during interaction with flowing atmospheres of argon, argon/oxygen and saturated argon. Test temperatures ranged between 600 and 1300°C. Analysis of the TG test results has shown that evaporation of the liquid boron oxide could be interpreted as combination of two processes: 1) direct evaporation of B_2O_3; 2) formation of the gaseous boric acids (in ortho- and meta- forms) in reaction of B_2O_3 with water molecules and their entrainment by the steam flow.

It was also found in the TG test program that these two mechanisms of boron oxide evaporation had different Arrhenius dependencies on temperature. Due to a strong temperature dependence of B_2O_3 evaporation, very high reaction rates were predicted for high temperatures, whereas indirect transport via boric acids would dominate at lower temperatures.

The temperature dependence of the direct B_2O_3 evaporation rate was evaluated in the TG tests [2] as:

$$r_{B_2O_3}^{max} = A \cdot \exp\left(\frac{-382900\ J/mol}{RT}\right), \qquad (57)$$

where R = 8.314 $J \cdot mol^{-1} \cdot K^{-1}$.

Since during the steady-state oxidation the B_4C is transformed into the boron oxide with the constant rate equal to the B_2O_3 evaporation rate, this temperature dependence can be considered as the specific reaction rate $\alpha(T)$ in the high temperature range, in which the direct evaporation of the boron oxide dominates.

In the lack of sufficient experimental data for the hydrogen release rate in the BOX Rig tests with the Framatome pellets at high temperatures (> 1200°C), this temperature dependence of $\alpha(T)$, Eq. (57), was tested in the SVECHA/QUENCH (S/Q) code. Indeed, only two tests with the improved test procedure for the Framatome pellets are available in this temperature range: BOX 10607 and BOX 10611.

For the low temperature range (<1100 °C), in which formation and subsequent evaporation of the boric acids are dominating in the oxidation kinetics, the activation energy of the oxidation process was deduced from a more regular set of experimental data collected in Table 10, using the least-square method.

Afterwards, superposition of the low- and high-temperature Arrhenius rates with trial pre-exponents were introduced in the B_4C oxidation module of the S/Q code, and some simulations were performed to attain the best correspondence between experimental and calculated hydrogen release rates. The result of this procedure is shown in Fig. 12.

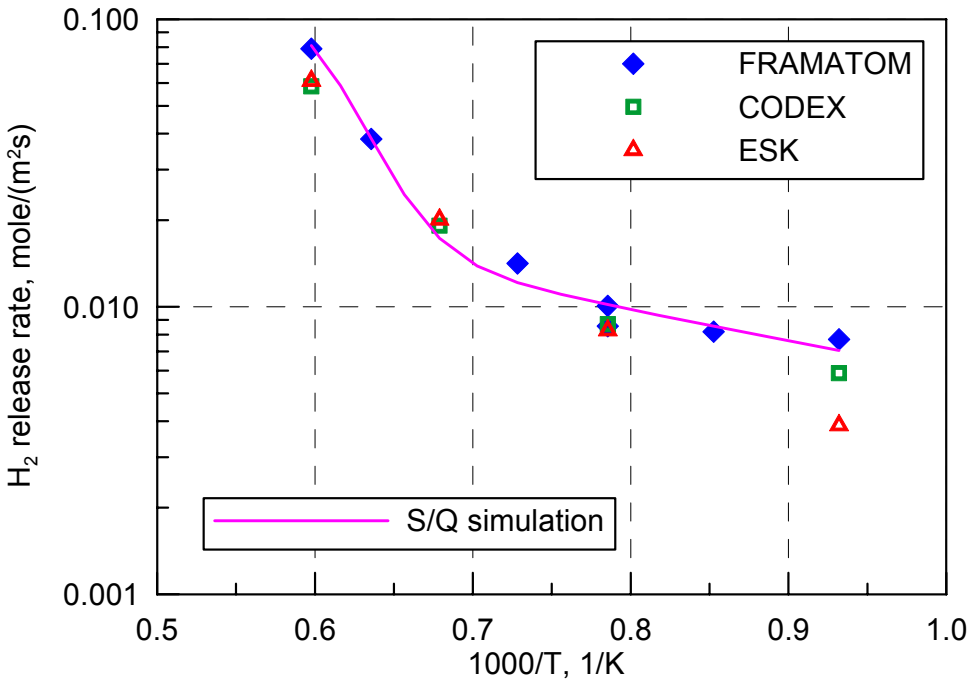

Fig. 12. S/Q simulation of hydrogen release rate during isothermal oxidation of Framatome B_4C pellet for the case of steam flow rate of 30 g/h and argon flow rate of 50 l/h.

Finally, the specific reaction rate $\alpha(T)$ in Eq. (1) can be best fitted in the form:

$$\alpha(T) = 2.5 \cdot 10^{-7} \cdot \exp\left(\frac{-21600}{RT}\right) + 6.0 \cdot 10^{5} \cdot \exp\left(\frac{-382900}{RT}\right). \quad (58)$$

The first term corresponds to the low temperature kinetics (< 1100°C) and the second one describes the rate of the chemical reaction at high temperatures (> 1200°C).

In Fig. 13 comparison of the measured and the calculated hydrogen release rates for all types of the pellets is plotted. One can see a good agreement of the calculated and measured values.

To verify the proposed approach, additional simulations of BOX Rig tests by the S/Q code were performed as presented below.

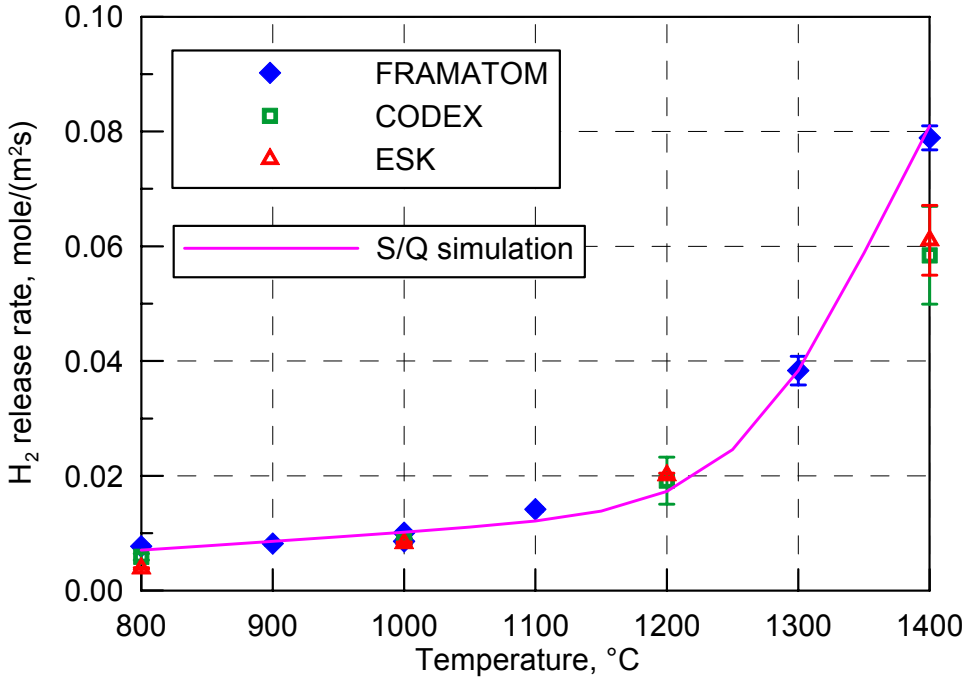

Fig. 13. Comparison of measured and S/Q simulation results of hydrogen release rate during isothermal oxidation of different type of B_4C pellet for the case of steam flow rate of 30 g/h and argon flow rate of 50 l/h.

4.2. Verification against tests with varying atmosphere

Two tests BOX 10115 and BOX 10126 under varying gas flow at constant temperature with reliable hydrogen release measurements were selected to verify B_4C oxidation model, see Table 11. The gas flows rates given in this Table are referred to 0°C and 1 bar. The hydrogen release rates were converted with the following equation [1]:

$$[H_2 \text{ release rate in l/h}] = [H_2 \text{ release rate in mole/(m}^2\text{s)}] \times F_{H2}\,, \quad (59)$$

where F_{H2} is the value of 30.03 in the case of Framatome pellets.

Both tests were carried out at constant temperature of 1200 °C with Framatome B_4C pellets. The only difference was the following: in the test BOX 10115 the argon flow rate was a

constant value of 50 l/h during the test and the steam flow rate was varied, while in the test BOX 10126 the steam flow rate of 30 g/h was constant and the argon flow rate was varied.

Test ID	Temperature	Argon	Steam	Specimen
	°C	ln/h	g/h	
10115	1200	50	5-70	Framatome
10126	1200	10-100	30	Framatome

Table 11. Test conditions of tests on B_4C oxidation in the BOX Rig under varying steam or argon flow rates.

In simulation of these tests with the S/Q code, the heat release due to B_4C oxidation was not taken into account. Validity of this approach is discussed below in Section 4.5.

Comparison of the experimental and S/Q simulation results for the hydrogen release rate in the tests BOX 10115 and BOX 10126 is presented in Figs. 14 and 15. Experimental data are plotted as the mean values and the standard deviations obtained after numerical treatment of the data. These standard deviations correspond to the hydrogen release scattering caused mainly by the gas supply system.

One can see from the plots that the S/Q predictions are in a good agreement with test data. The model of B_4C oxidation correctly describes the dependence of the hydrogen release rate on the gas flow. The maximum deviation of the predicted and measured values is observed at very low or very high gas flow rates. A possible reason may be an increased inaccuracy of the gas release measurements in such conditions.

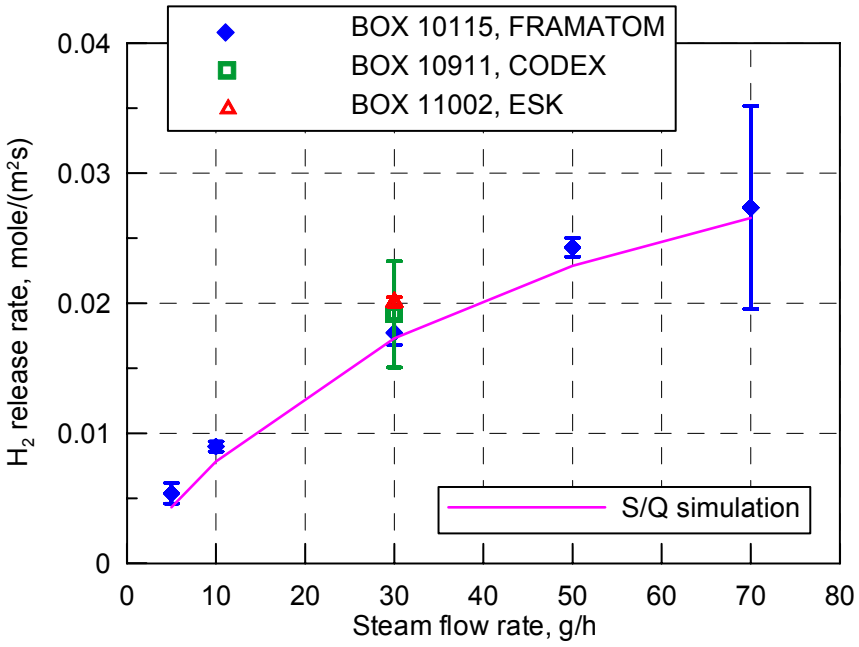

Fig. 14. Comparison of measured and S/Q simulation results for hydrogen release rate during oxidation of Framatome B_4C pellet at 1200°C in argon/steam in the test BOX 10115. Variation of steam flow rate.

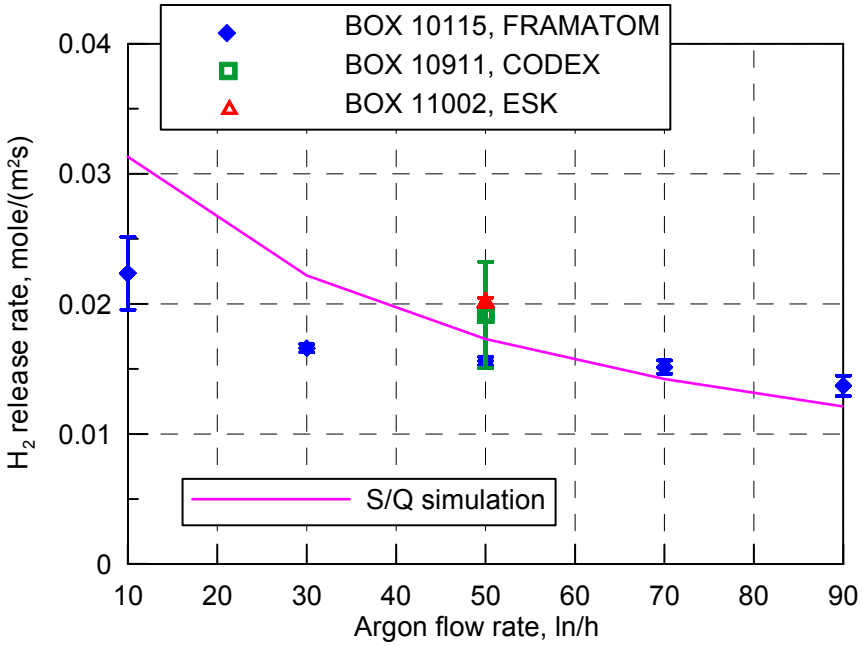

Fig. 15. Comparison of measured and S/Q simulation results for hydrogen release rate during oxidation of Framatome B_4C pellet at 1200°C in argon/steam in the test BOX 10126. Variation of argon flow rate.

4.3. Verification against isothermal tests with reduced steam flow rate

Another test series was performed with 10 times lower steam flow rate (3 g/h instead of 30 g/h). The Framatome and ESK pellets were tested. The obtained in [1] oxidation rates are converted in hydrogen release rates in accordance with Eq. (56) and presented in Table 12. The test at 800 °C had a long duration of one hour, in order to attain equilibrium (plateau) state. The initial peaks in gas release are considerably broader in comparison with ones in the tests with higher steam flow rates, and it took more time to reach a constant oxidation rate [1]. Furthermore, the absolute values of gas release are about four times lower in the test series with reduced steam injection.

Test ID	Temperature	Argon	Steam	Specimen	H_2 release rate
	°C	ln/h	g/h		mole/m^{2}s
20304	800	50	3	Framatome	0.001680
20409	800	50	3	ESK pellet	0.000616
20305	1000	50	3	Framatome	0.00136
20410	1000	50	3	ESK pellet	0.00112
20306	1200	50	3	Framatome	0.00568
20411	1200	50	3	ESK pellet	0.00432
20313	1400	50	3	Framatome	0.02320
20416	1400	50	3	ESK pellet	0.01600

Table 12. Test conditions and results of isothermal experiments on B_4C oxidation in the BOX Rig under reduced steam flow rate of 3 g/h and argon flow rate of 50 l/h.

Comparison of the experimental and simulated hydrogen release rates is presented in Fig. 16. The test temperature was assumed to be constant during the tests, and heat release due to B_4C oxidation was not taken into account. One can see that for the low temperature range (< 1100°C) the S/Q code gives a good prediction of the hydrogen release rate, while for high temperatures (> 1200°C) the S/Q code underestimates the hydrogen release.

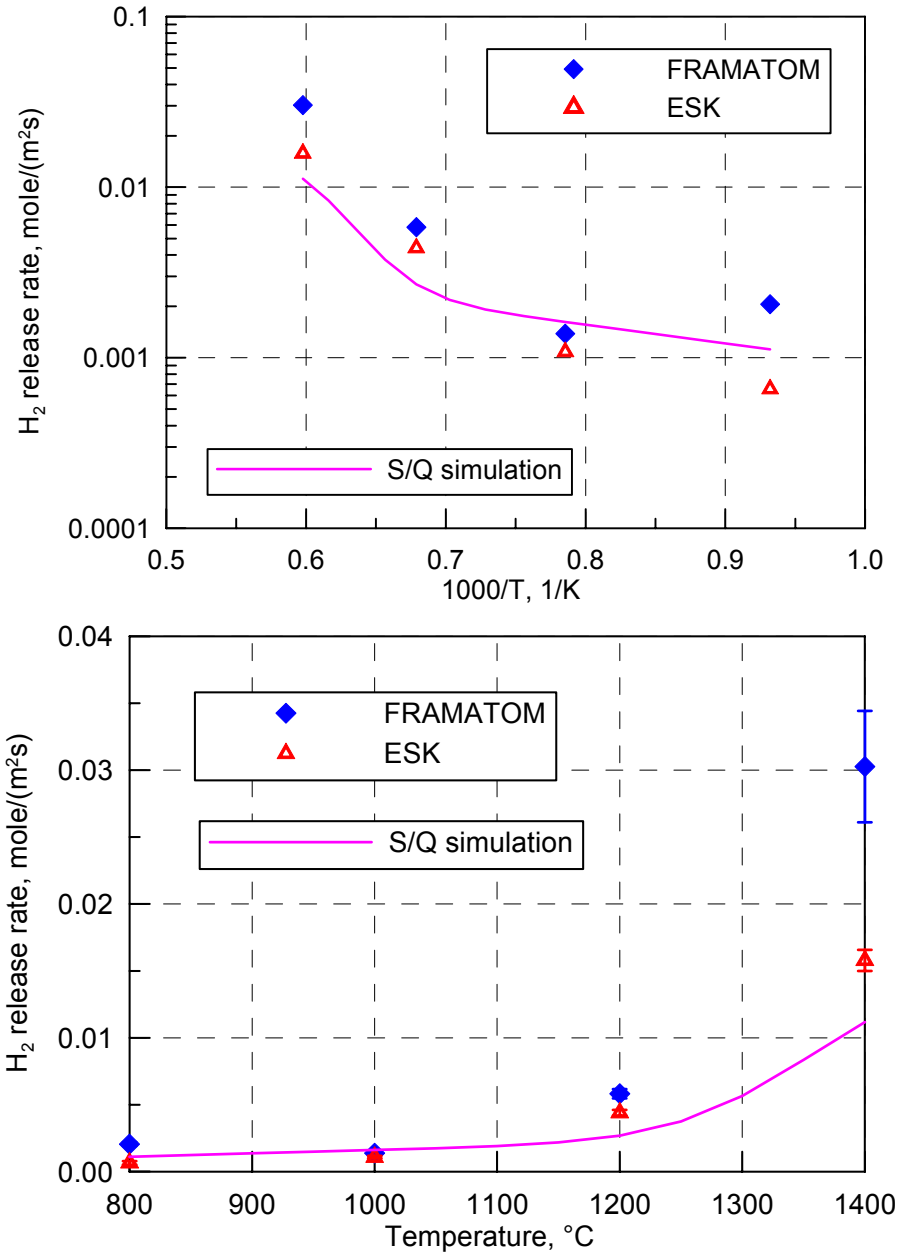

Fig. 16. Comparison of measured and S/Q simulation results for hydrogen release rate during isothermal oxidation of Framatome and ESK B_4C pellets for the case of reduced steam flow rate of 3 g/h and argon flow rate of 50 l/h.

4.4. Verification against transient temperature tests

Several tests under transient temperature conditions were carried out in the Box Rig, however, only one test BOX 10406 was carried out in the improved test conditions (see Fig. 4 in Section 2.2). Conditions of this test are presented in Table 13.

Test ID	Temperature	Argon	Steam	Specimen
	°C	ln/h	g/h	
10406	800-1500	50	30	Framatome

Table 13. Test conditions of transient temperature test on B_4C oxidation in the BOX Rig in argon/steam mixture.

It should be noted that the off-gas pipe was blocked during cool-down [1], therefore, the S/Q simulation of this test was performed for the heat up stage. The test conditions and measured gas release in the test BOX 10406 are presented in Fig. 17. Hydrogen release rate as a function of time was obtained converting the measured values in accordance with Eq. (59).

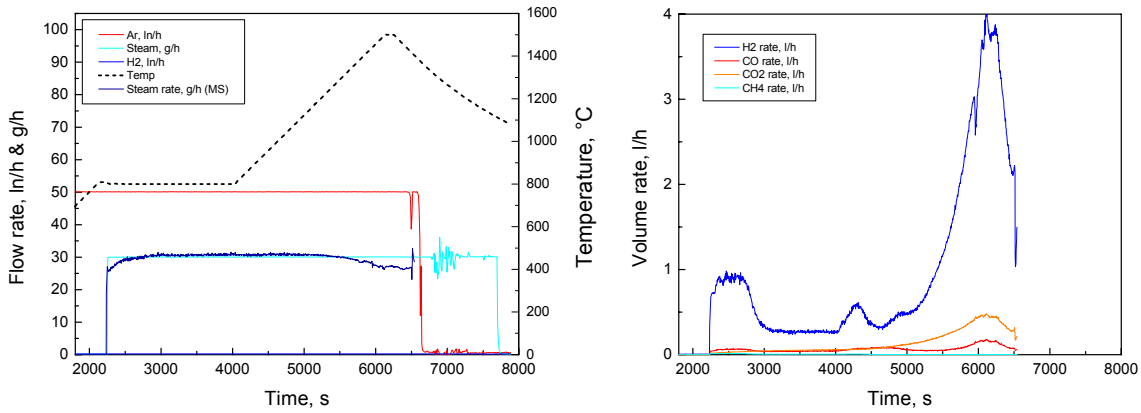

Fig. 17. Test conditions and measured gas release rate in the test BOX 10406. Transient temperature oxidation of Framatome B_4C pellet under steam flow rate of 30 g/h and argon flow rate of 50 l/h.

Comparison of the measured and S/Q simulation results for the hydrogen release rate in the test BOX 10406 is presented in Fig. 18. In addition, results measured in the plateau phase of the isothermal tests from Table 10, are also plotted in Fig. 18. One can see that in the beginning of the transient test BOX 10406 (< 5000 s) the measured values considerably exceed the calculated ones, since at low temperatures (800-900 °C) it takes a long time to achieve a steady state release. Afterwards as temperature rises the steady state phase is attained rather quickly, and the measured and the calculated hydrogen release rates are in a good agreement. Nevertheless, it should be noted that the experimental values in the test BOX 10406 are somewhat higher than ones in the isothermal tests. Good agreement among experimental and calculated values retains up to the temperature of ~ 1400 °C, and then the difference increases.

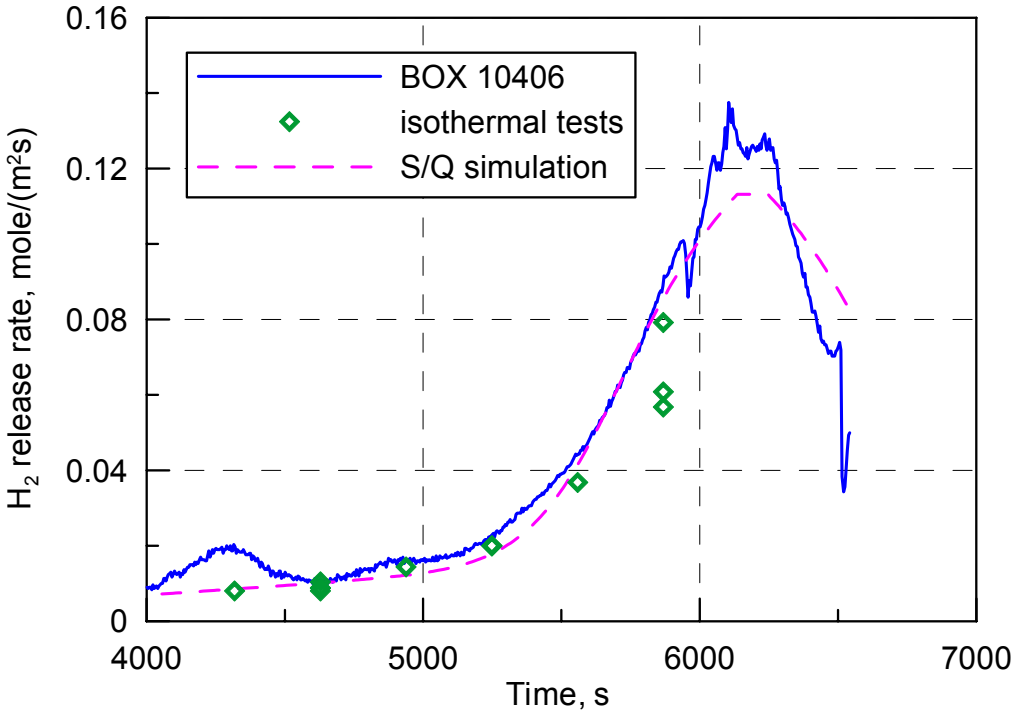

Fig. 18. Comparison of measured and S/Q simulation results for hydrogen release rate during transient temperature oxidation of Framatome B_4C pellet in the test BOX 10406.

4.5. Verification against measurements of minor gaseous products release

Despite the mass spectrometer allows the quantitative analysis of all gaseous reaction products, the hydrogen measurements are the most reliable and may be used as a continuous measure for the B_4C oxidation kinetics. There are some difficulties for the accurate quantitative measurement of the other gaseous products [1]. Intensities of the mass spectrometer peaks indicate which masses may be quantitatively analysed. Carbon monoxide CO and nitrogen N_2 have their main peaks at the same mass 28. Therefore, one should be sure that nitrogen is not present in the system. Furthermore, there is an overlapping of peaks from carbon dioxide CO_2 and metaboric acid HBO_2 at the mass 44. This may also lead to an inaccuracy in measurements of CO and CO_2.

Besides, boric acids production could only be measured qualitatively due to a missing calibration method and partial condensation in the off gas system.

And finally, as indicated in Section 2.1 the off-gas tube from the furnace to the mass spectrometer is heated to about 150 °C to prevent steam condensation, therefore, there is a possibility of chemical transformation in the off-gas system, whereas the presented simulations describe the gas content at the test temperatures. In more details this effect will be described below in Section 5.2.

Taking into account these features, one may conclude that the measurements of the minor gaseous products (with except of hydrogen) can be considered only as semi-quantitative. Nevertheless, it is interesting to compare the measured and the predicted values. In this part of the paper simulations with S/Q of the gaseous products release due to the B_4C oxidation are presented. Calculations were performed for all test conditions; however, the most typical ones are presented below. Standard deviations plotted in the figures correspond to dispersion of measured values in a single test, similarly to the above presented calculations of the hydrogen release rate.

In Fig. 19 comparison of measured and S/Q simulation results for the carbon dioxide steady-state release rate during isothermal oxidation is presented for the case of steam flow rate of 30 g/h and argon flow rate of 50 l/h. As for the case of hydrogen, the carbon dioxide release rate is predicted rather satisfactory, and a pronounced dependence from the temperature is reproduced.

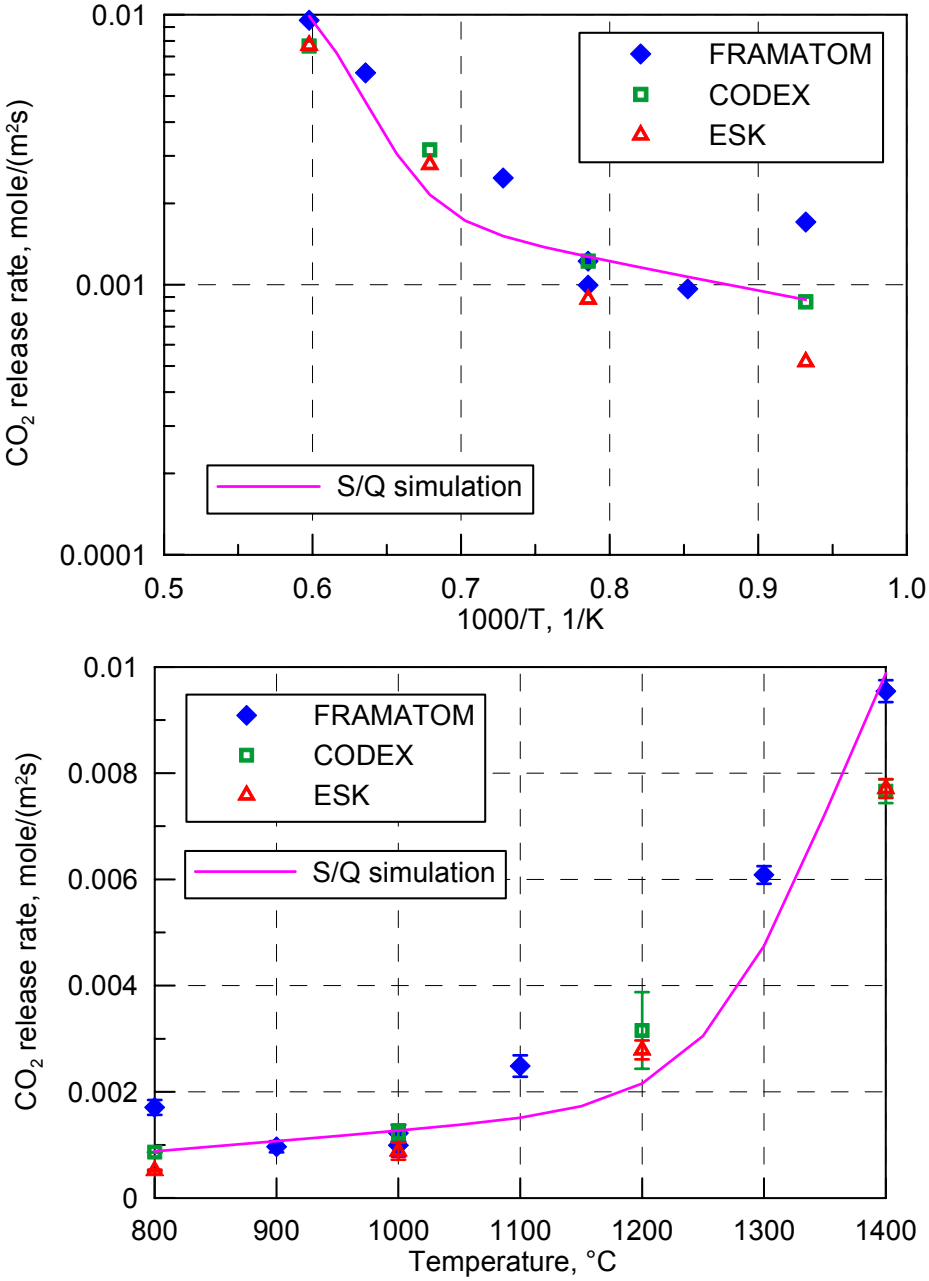

Fig. 19. Comparison of measured and S/Q simulation results for the carbon dioxide steady-state release rate during isothermal oxidation of different types of B_4C pellets for the case of steam flow rate of 30 g/h and argon flow rate of 50 l/h.

For carbon monoxide and methane the experimental data do not demonstrate a clear dependence from temperature, Figs. 20 and 21. Probably, this is a consequence of the above mentioned low accuracy of these minor components measurements. The S/Q code strongly underestimates the release rates, especially for methane, this can be also explained by mutual transformations of the carbon containing species on cool-down, however, the code correctly predicts the total amount of the released carbon.

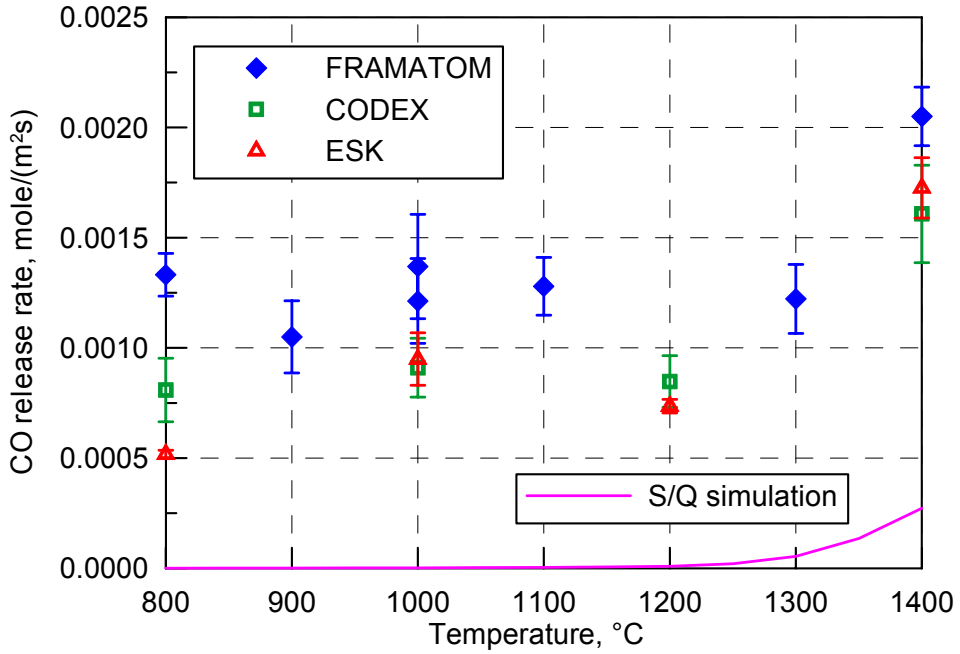

Fig. 20. Comparison of measured and S/Q simulation results for the carbon monoxide steady-state release rate during isothermal oxidation of different types of B_4C pellets for the case of steam flow rate of 30 g/h and argon flow rate of 50 l/h.

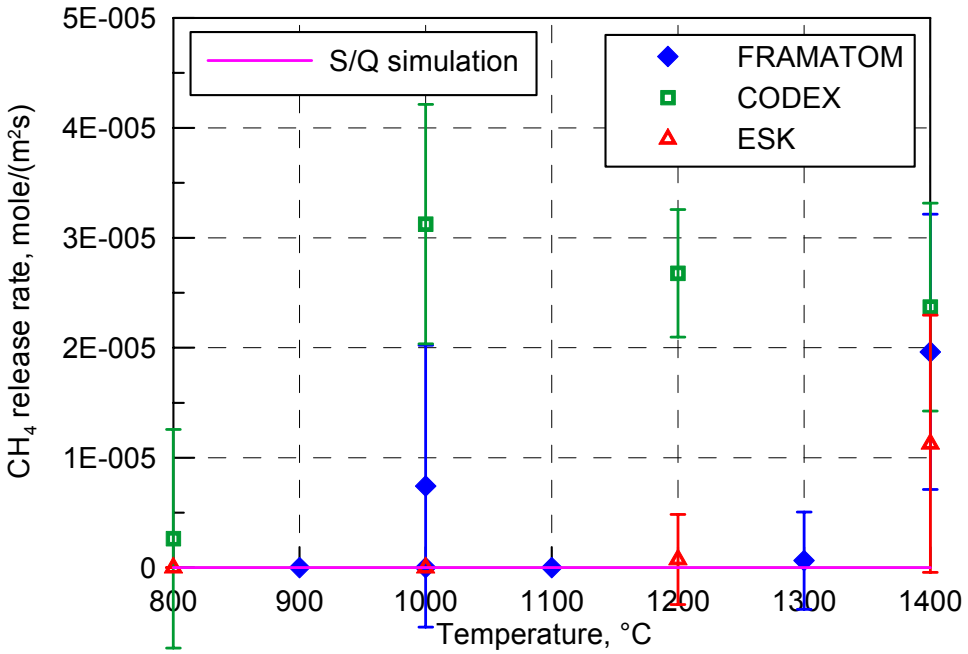

Fig. 21. Comparison of measured and S/Q simulation results for the methane steady-state release rate during isothermal oxidation of different types of B_4C pellets for the case of steam flow rate of 30 g/h and argon flow rate of 50 l/h.

The S/Q simulation of the orthoboric (H_3BO_3), metaboric (HBO_2) acids, trimer of metaboric acid ($H_3B_3O_6$) and boron oxide (B_2O_3) steady-state release rates during isothermal oxidation is presented in Figs. 22 and 23, correspondingly. The code predicts a switch from orthoboric acid formation at lower temperatures to metaboric acid formation accompanied with increased evaporation of boron oxide at higher temperatures.

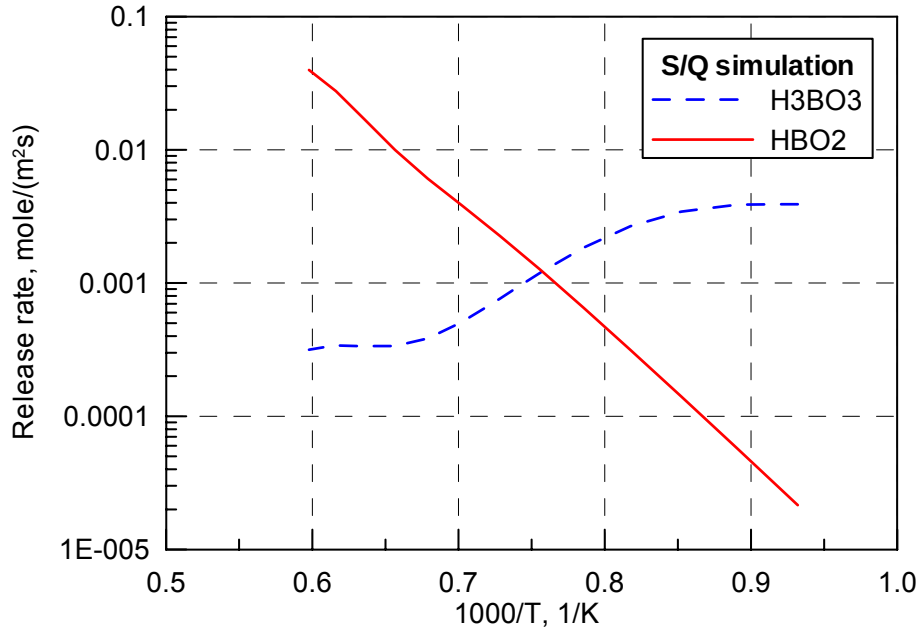

Fig. 22. S/Q simulation of the orthoboric (H_3BO_3) and metaboric (HBO_2) acids steady-state release rates during isothermal oxidation of B_4C pellets for the case of steam flow rate of 30 g/h and argon flow rate of 50 l/h.

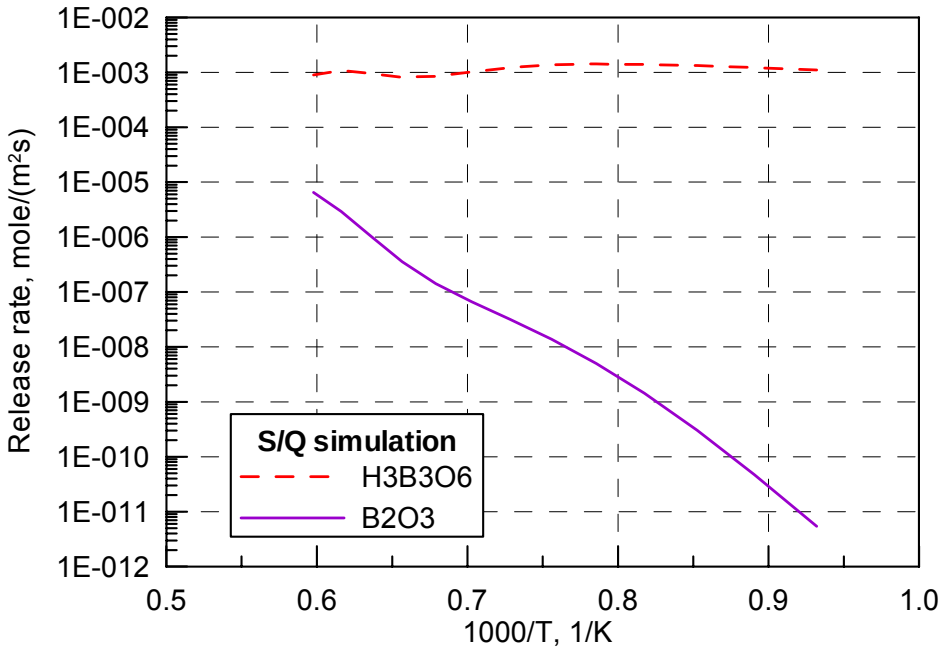

Fig. 23. S/Q simulation of the boron oxide (B_2O_3) and the trimer of metaboric acid ($H_3B_3O_6$) steady-state release rates during isothermal oxidation of B_4C pellets for the case of steam flow rate of 30 g/h and argon flow rate of 50 l/h.

Figs. 24-26 present the comparison of the measured and S/Q simulation results for the carbon dioxide, carbon monoxide and methane steady-state release rates during isothermal oxidation in the case of reduced steam flow rate of 3 g/h and argon flow rate of 50 l/h. One can see the same tendencies as for the above case of the steam flow rate of 30 g/h and argon flow rate of 50 l/h: a good agreement of the measured

and calculated release rates for carbon dioxide, code underestimation of the carbon monoxide and methane release rates in the lack of a clear dependence of the latter measurements from temperature.

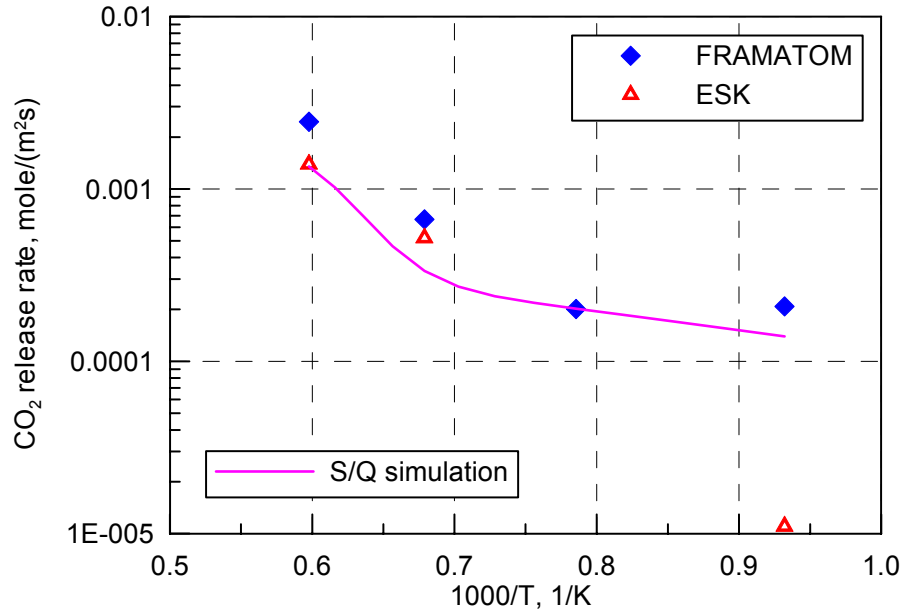

Fig. 24. Comparison of measured and S/Q simulation results for the carbon dioxide steady-state release rate during isothermal oxidation of Framatome and ESK B_4C pellets for the case of reduced steam flow rate of 3 g/h and argon flow rate of 50 l/h.

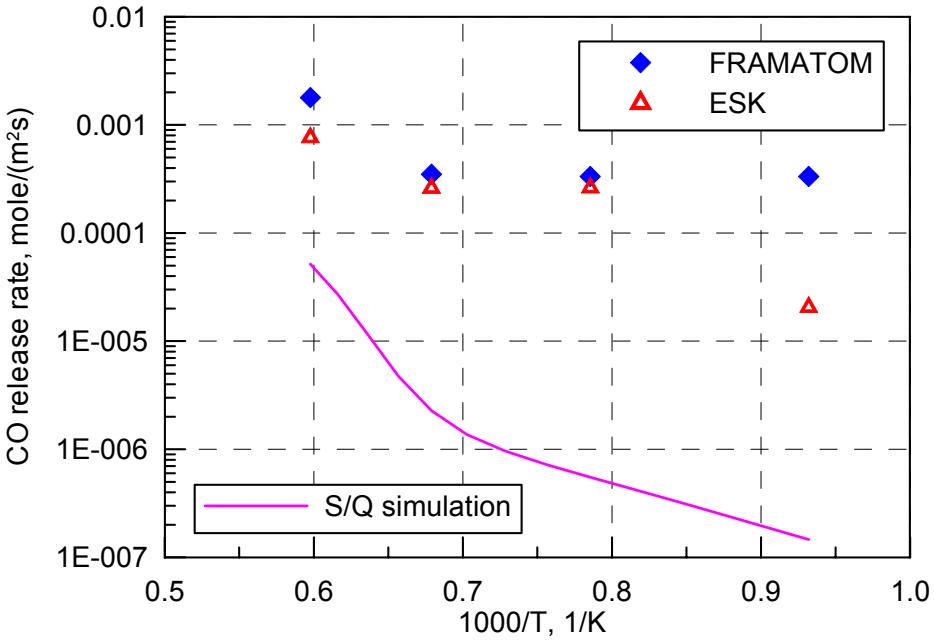

Fig. 25. Comparison of measured and S/Q simulation results for the carbon monoxide steady-state release rate during isothermal oxidation of Framatome and ESK B_4C pellets for the case of reduced steam flow rate of 3 g/h and argon flow rate of 50 l/h.

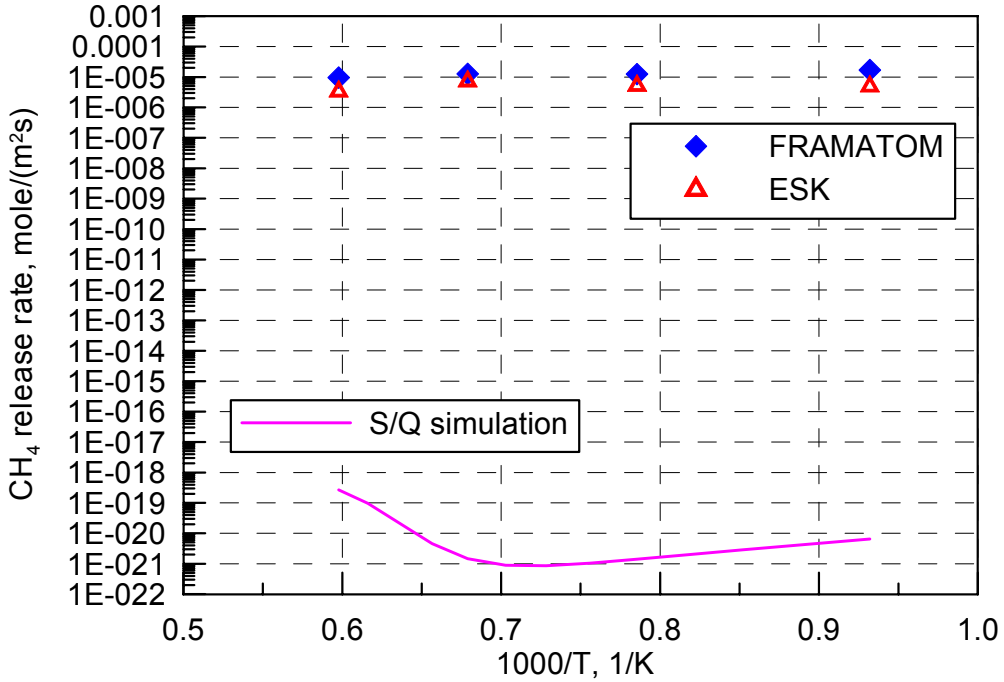

Fig. 26. Comparison of measured and S/Q simulation results for the methane steady-state release rate during isothermal oxidation of Framatome and ESK B_4C pellets for the case of reduced steam flow rate of 3 g/h and argon flow rate of 50 l/h.

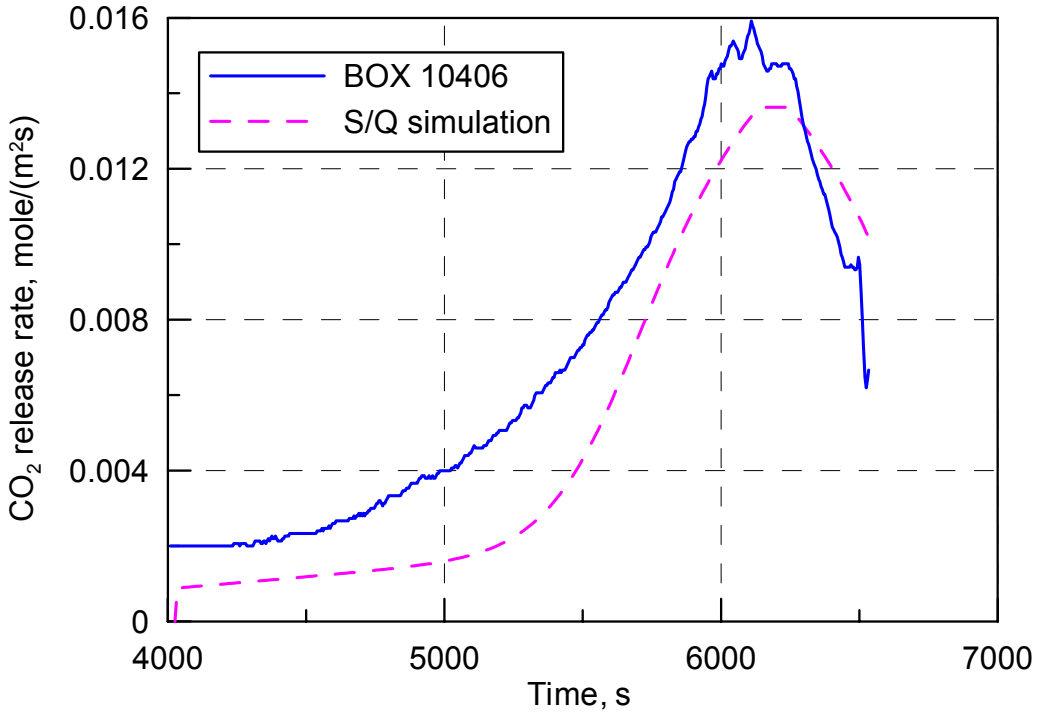

Fig. 27. Comparison of measured and S/Q simulation results for the carbon dioxide release rate during transient temperature oxidation of Framatome B_4C pellet in the test BOX 10406.

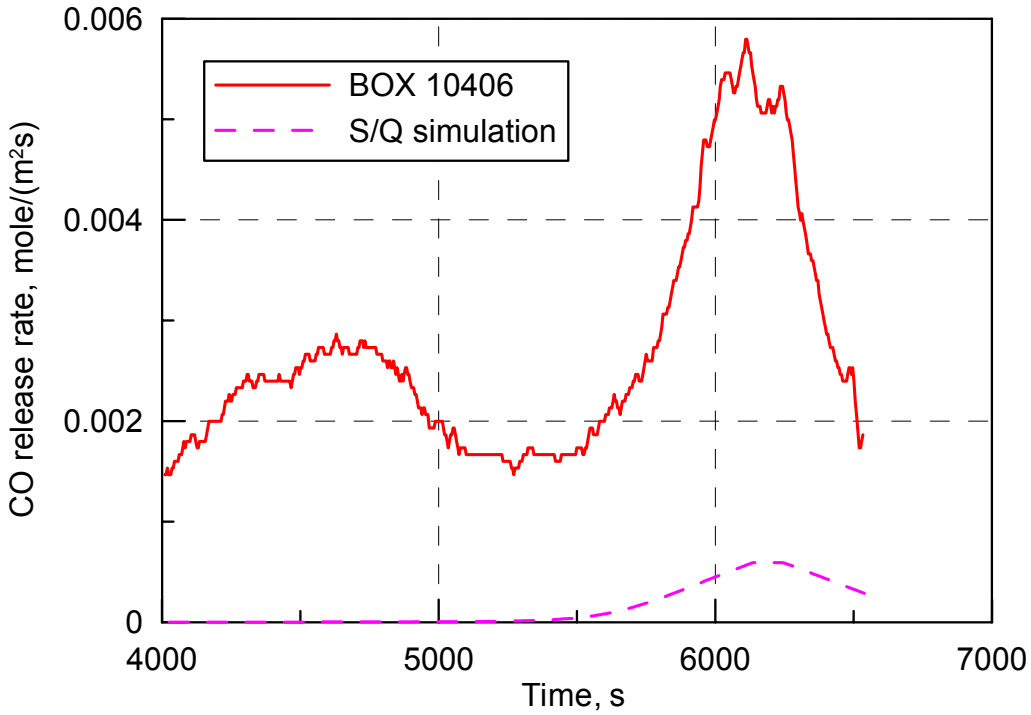

Fig. 28. Comparison of measured and S/Q simulation results for the carbon monoxide release rate during transient temperature oxidation of Framatome B_4C pellet in the test BOX 10406.

The same tendencies are observed in transient tests. In Figs. 27 and 28 the comparison of measured and S/Q simulation results for the carbon dioxide and monoxide release rates during transient temperature oxidation in the test BOX 10406 is plotted.

4.6. Heat effect of B_4C oxidation

Investigation of the heat release owing to B_4C oxidation by steam at high temperatures and its possible influence on the oxidation kinetics owing to temperature escalation on the reaction surface can be performed using the S/Q code with tight coupling of the heat and mass transfer modules with the newly implemented B_4C oxidation module.

The main model assumptions are the following:

- Only steam and argon as the dominant gases are taken into consideration in the heat and mass transfer modules.
- Temperature of the furnace wall in the test simulations is invariable with time and uniformly distributed along axial direction. Inlet gas temperature is the same as the temperature of the furnace wall.
- Thermal properties of the boron carbide such as the specific heat capacity and thermal conductivity are taken from MATPRO data base [12]. Since the emissivity of liquid boron oxide is not available, a trial value of 0.5 is used in the calculations. The real density of Framatome pellets is used.
- The heat release of B_4C oxidation reaction is chosen as $382.9 \cdot 10^3$ J/mol of the oxidised boron carbide [13]. The energies of the direct boron oxide evaporation and the boric

acids formation are not available and thus neglected in calculations. This allows a conservative estimation (i.e. the upper limit) of the heat effect.

- The boron carbide oxidation heat is released on the pellet surface.

Two high temperature isothermal tests BOX 10607 and BOX 10611 from Table 10 were selected for simulation of the B_4C oxidation heat release effect. The test conditions and measured gas release in these tests are presented in Figs. 29 and 32, correspondingly.

Since the B_4C oxidation module of the S/Q code calculates the oxidation rate after attainment of the steady state, it does not allow evaluation of the heat release in the short initiation (transient) period. To evaluate the influence of the initiation period and to verify the heat release prediction by the code, the experimental heat release history was deduced from the hydrogen release measurements. After that, for each test two types of simulations were performed. In the first simulation the heat deduced from the experiment was released on the surface of the pellet, and in the second simulation the heat self-consistently calculated by the oxidation module of the S/Q code was used.

The pellet surface temperature evolution at the pellet half height elevation is presented in Figs. 30 and 33, correspondingly. One can see that calculations with the experimental heat release give a sharp temperature peak in the short initiation period before stabilisation of the steady state temperature. Owing to the above presented limitation of the S/Q oxidation module, the second type of calculations based on the self-consistent calculation of the heat release does not reproduce this sharp temperature peak, however, predicts the steady state temperature in a reasonable agreement with the first type of calculations. In both types of calculations the temperature increase due to B_4C oxidation in the steady state stage is not significant and attains ≈ 5 degrees at test temperature 1300 °C and ≈ 10 degrees at test temperature 1400 °C.

Influence of heat up effect due to oxidation on the hydrogen release is presented in Figs. 31 and 34 at temperatures 1300 and 1400 °C, correspondingly. One can see that the effect is negligible. The obtained results confirm reliability of the calculation results obtained above without taking the heat release into consideration.

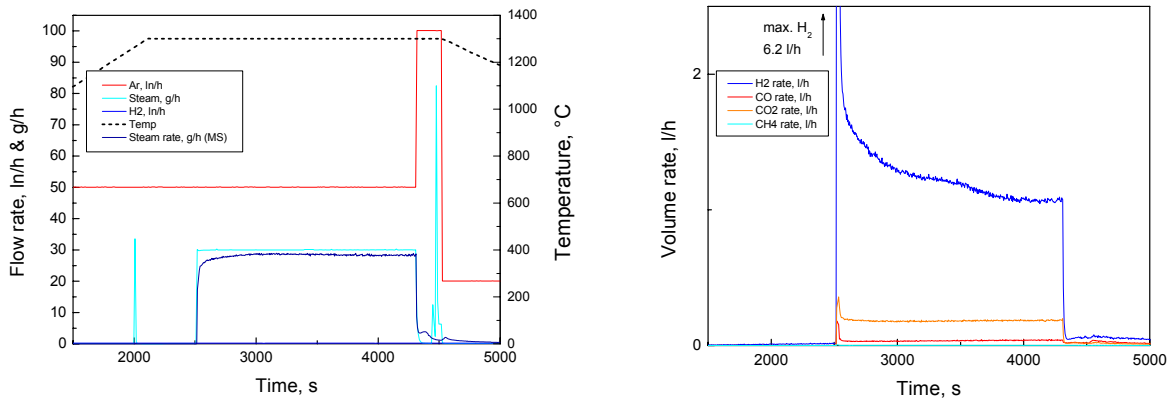

Fig. 29. Test conditions and measured gas release rate in the test BOX 10607. Isothermal oxidation of Framatome B_4C pellet in argon/steam at 1300 °C.

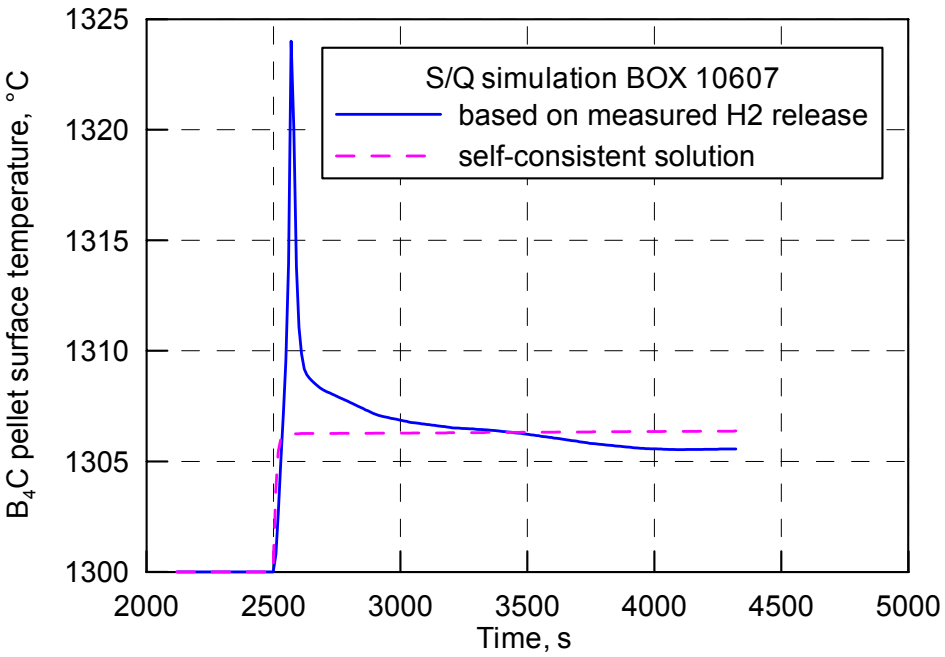

Fig. 30. S/Q simulation of Framatome B_4C pellet heat up due to B4C oxidation in the test BOX 10607. Comparison of self-consistent and based on measured hydrogen release solutions.

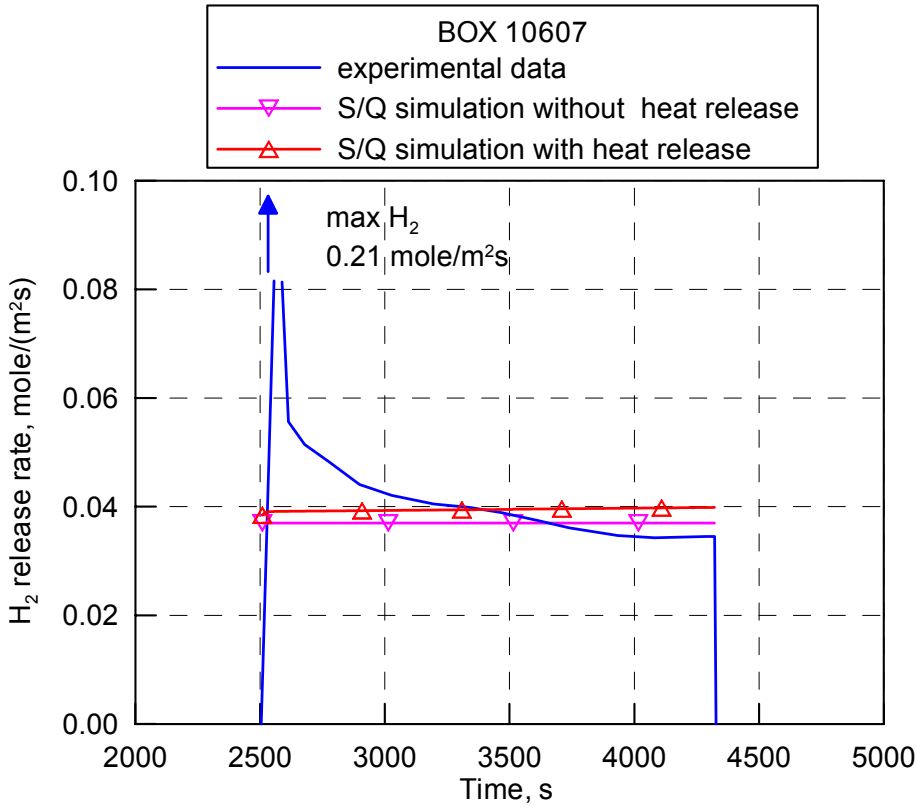

Fig. 31. Comparison of measured and S/Q simulation (with and without consideration of heat release) results for hydrogen release rate during isothermal oxidation of Framatome B_4C pellet in the test BOX 10607.

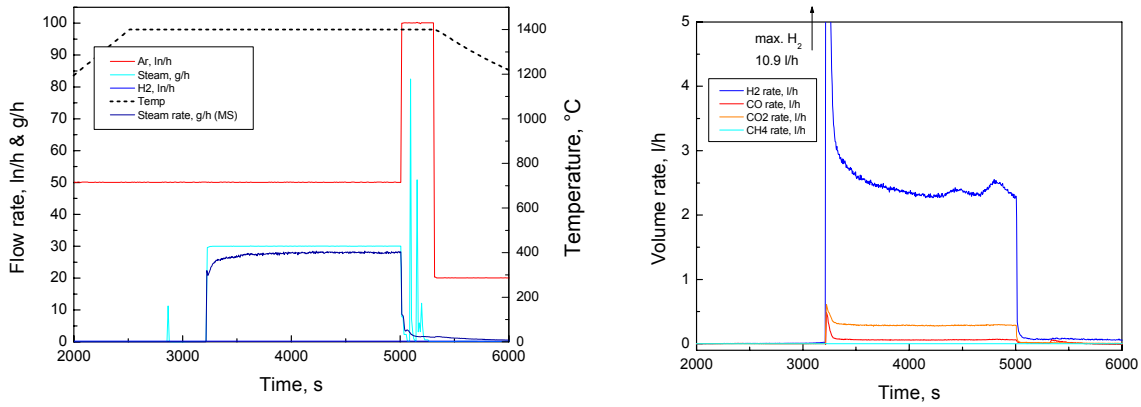

Fig. 32. Test conditions and measured gas release in the test BOX 10611. Isothermal oxidation of Framatome B_4C pellet in argon/steam at 1400 °C.

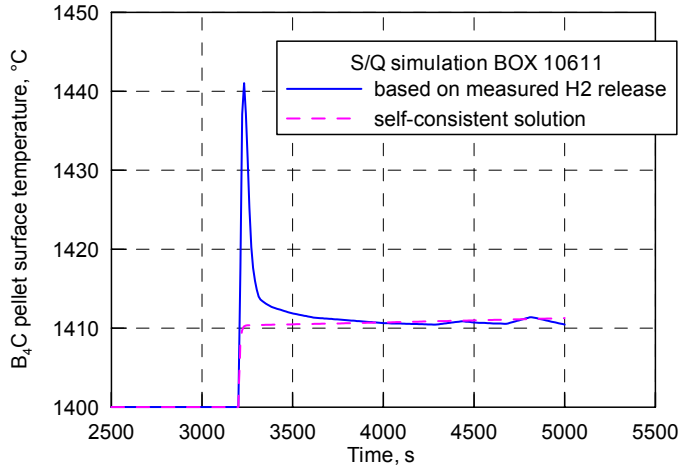

Fig. 33. S/Q simulation of Framatome B_4C pellet heat up due to B4C oxidation in the test BOX 10611. Comparison of self-consistent and based on measured hydrogen release solutions.

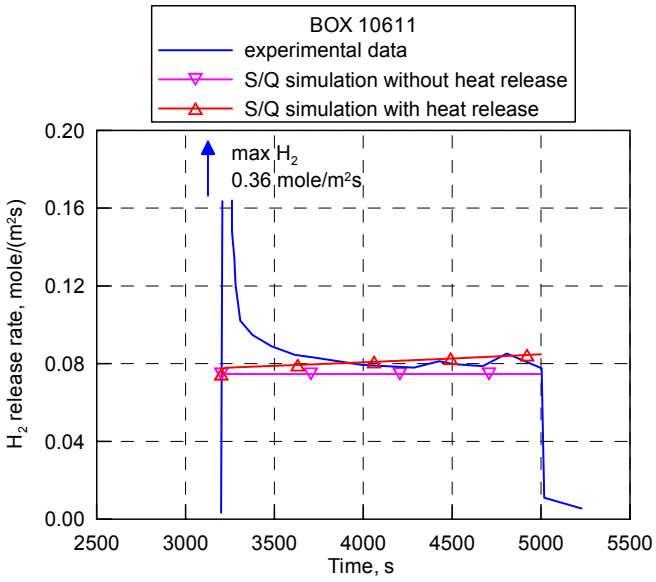

Fig. 34. Comparison of measured and S/Q simulation (with and without consideration of heat release) results for hydrogen release rate during isothermal oxidation of Framatome B_4C pellet in test BOX 10611.

5. Model predictions for future tests

5.1. Determination of various kinetic regimes

At each temperature one can distinguish two kinetic regimes: at low gas flow velocities mass transfer in the gas phase controls oxidation rate, and at high gas velocities the surface reaction rate becomes rate controlling process. As follows from the experimental data (see Section 2.2), at least at temperatures above 1200°C the BOX Rig tests were conducted in the transition kinetic region where the rate of the gas phase mass transfer is comparable with the rate of the surface chemical reaction. In order to determine critical gas flow velocities separating the two kinetic regions, the following calculations have been carried out:

In calculations bulk hydrogen partial pressure was fixed along with the Ar/H_2O ratio of injected gas mixture, and gas flow velocity was varied by proportional increase of argon and steam flow rates. For future tests a relatively high ratio $Ar[l/h]:H_2O[g/h]=5$ is proposed in order to reduce influence of the oxidation reaction heat production on the specimen temperature, on the one hand, and to simplify gas phase mass transfer modelling, on the other hand. According to the calculation results, at 1000 °C H_2 gas flow velocities about 0.2 m/s are sufficiently high to observe oxidation rates independent on gas phase mass transfer (i.e. controlled by surface reaction rate), Fig. 35. At 1200 °C transition to the kinetic regime purely controlled by the surface reaction rate occurs at gas flow velocity ~ 0.5 m/s, Fig. 36. At 1400 °C mass transfer in the gas phase, according to the calculations, considerably slows down (and thus controls) the B_4C oxidation process at high gas flow velocities typical for reactor conditions ~ 1 m/s, Fig. 37. With further temperature elevation the oxidation rate dependence on the flow velocity becomes more pronounced, Fig. 38.

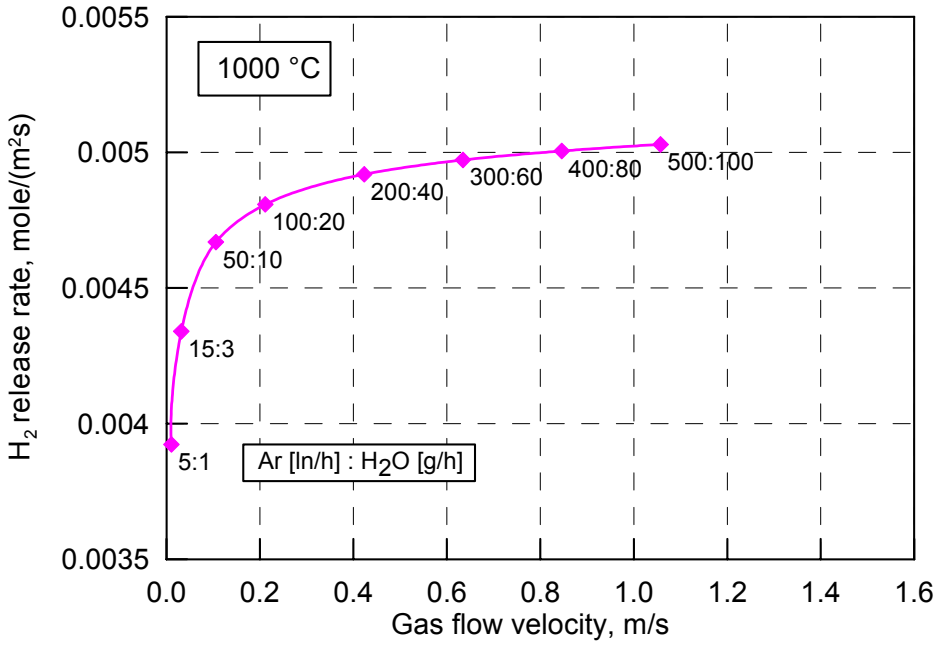

Fig. 35. Dependence of hydrogen production rate on gas flow velocity at 1000°C and P_{H_2O} = const.

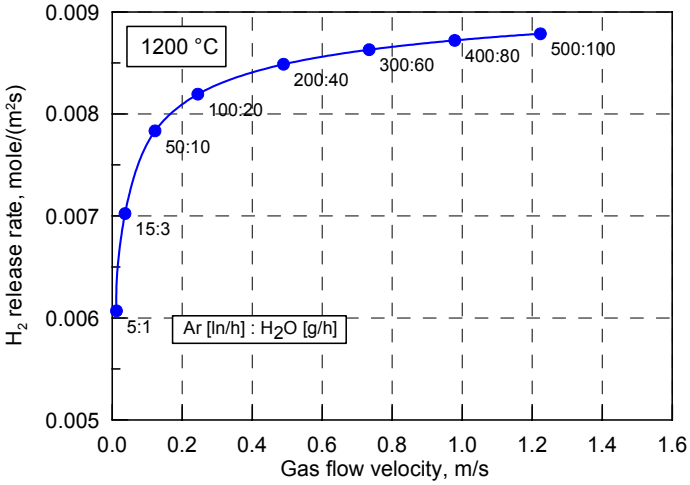

Fig. 36. Dependence of hydrogen production rate on gas flow velocity at 1200°C and P_{H_2O} =const.

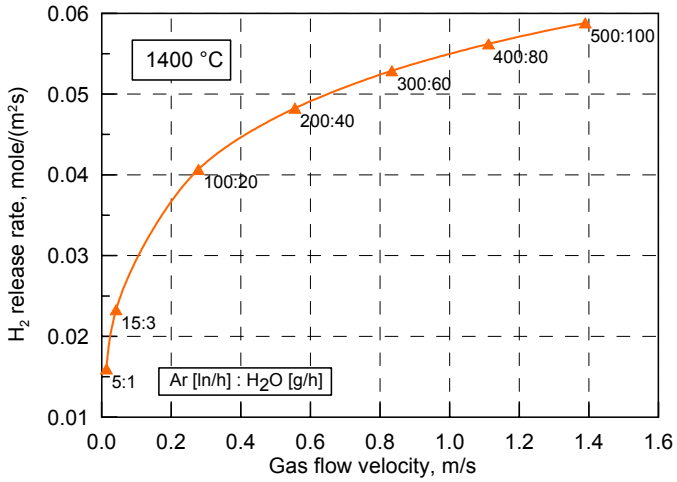

Fig. 37. Dependence of hydrogen production rate on gas flow velocity at 1400°C and P_{H_2O} =const.

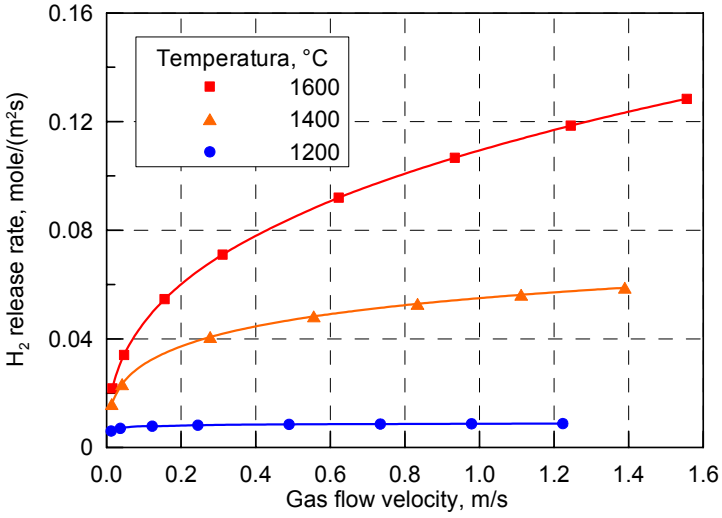

Fig. 38. Dependence of hydrogen production rate on gas flow velocity with temperature increase from 1200 to 1600°C and P_{H_2O} =const.

5.2. Methane generation on cool-down of the outlet reaction gas mixture

As indicated in Section 2.1, the off-gas tube from the furnace to the mass spectrometer (MS) is heated to about 150 °C to prevent steam condensation. For this reason, it might be necessary to recalculate the outlet gas composition taking into account possible chemical transformations of the gaseous B_4C oxidation products on cool-down from the test temperature to the temperature of the off-gas tube.

Such calculations were attempted with the S/Q code in order to predict the gas composition on cool-down; however, an additional analysis with the IVTAN-Thermo software [6] shows that a noticeable condensation of the metaboric acid HBO_2 occurs if the off-gas mixture is cooled down below ≈ 700 K to its thermodynamically equilibrium state. These calculations also show that below ≈ 450 K the gases CO and CO_2 will be almost completely transformed into CH_4 along with further condensation of the metaboric acid HBO_2 if the equilibrium state of the outlet gas mixture will be attained, see Fig. 39.

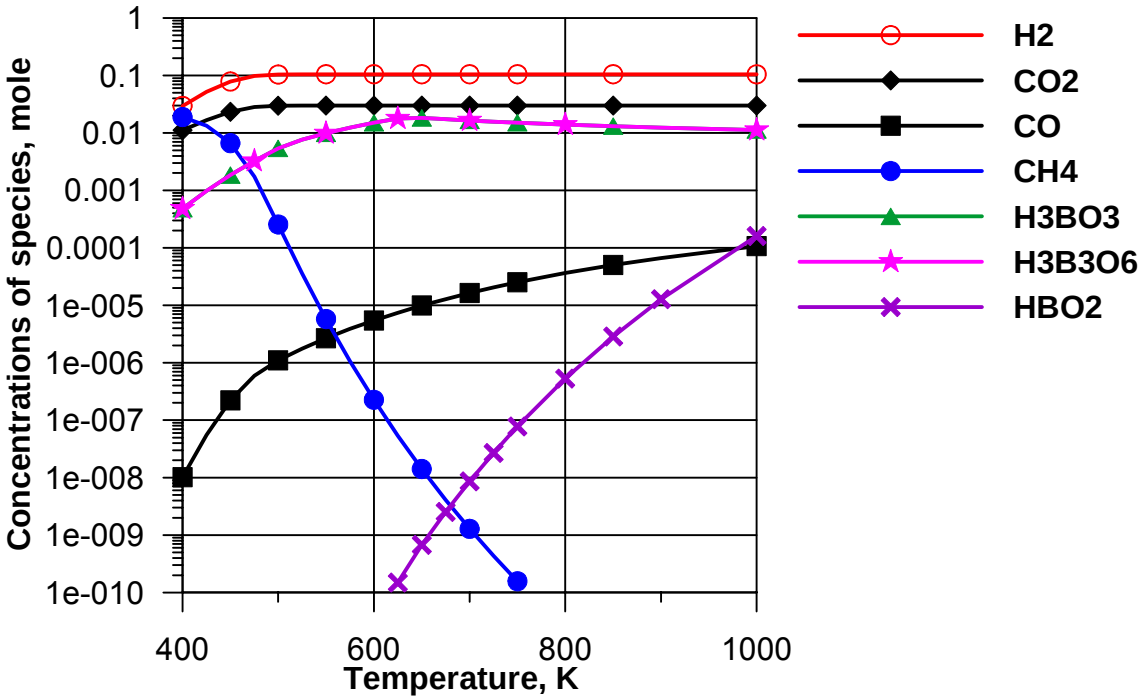

Fig. 39. Equilibrium concentrations of dominating gaseous products of the B_4C oxidation reaction on cool-down of the outlet gas mixture, calculated with the IVTAN-Thermo software.

This implies that the S/Q code cannot be directly applied to consideration of the cool-down effect, since no condensed phases (which appear at relatively low temperatures ≤ 600 K) are considered in the current version of the oxidation model (see Section 3.1). On the other hand, the equilibration process of the gas mixture on cool-down can be much longer in comparison with the relatively short cooling process. In this case, the measured by MS gas composition might be different from the IVTAN-Thermo equilibrium state predictions.

As above mentioned, in some BOX Rig tests the off-gas pipe was really blocked during cool-down by condensed phases and simultaneously a noticeable methane production was detected, in contradiction with the model predictions for the test temperatures (presented in Section 4). However, the measured methane amounts were substantially lower than predicted by the equilibrium state calculations at MS temperature. Apparently this implies that the predicted CO and CO_2 transformation into CH_4 was really started in the off-gas tube,

however, was not completed (to its final equilibrium state) owing to a relatively short period of the cool-down process.

Furthermore, a negligible amount of measured CH_4 in comparison with CO and CO_2 allows quantitative comparison of the calculated and measured total amount of the carbon containing gases CO and CO_2 (rather than their separate amounts). Such a procedure will be performed in simulation by the S/Q code of the bundle test QUENCH-07 test with the central B_4C absorber rod in Section 6.

It is recommended to check experimentally the important prediction concerning methane production and to perform additional tests with a slow cool-down of the off-gas mixture, in order to avoid hazardous scenarios of severe accidents at NPP with methane production in cool zones of the reactor system.

6. Application of the SVECHA/QUENCH code with the newly implemented B_4C oxidation model to simulation of the QUENCH-07 bundle test

6.1. QUENCH-07 bundle test

The Q-07 test was performed in order to investigate the effect of B_4C oxidation and absorber rod failure on fuel bundle degradation. This test was expected to provide information about the formation of gaseous reaction products during absorber rod degradation and B_4C oxidation, in particular of H_2, CO, CO_2 and CH_4 and on the impact of control rod degradation on surrounding fuel rods [14-16].

The Q-07 test bundle consisted of 21 rods, 20 of which were electrically heated over a length of 1024 mm. The Zircaloy-4 rod cladding and the grid spacers were identical to those used in Western-type LWRs whereas the fuel was represented by ZrO_2 pellets. The central rod was made of an absorber rod with B_4C pellets and stainless steel cladding, and of a Zircaloy-4 guide tube.

During the test 3 g/s of superheated steam and 3 g/s of argon as carrier gas entered the test bundle at the bottom and exited at the top together with oxidation reaction products. Failure of the absorber rod cladding was detected at ~ 1585 K. After a B_4C oxidation phase at ~ 1720-1780 K and a subsequent transient test phase to well above 2000 K, cooling of the test bundle was accomplished by injecting saturated steam (mass flow rate 15 g/s) at the bottom of the test section.

The presence of the B_4C absorber material in the central rod triggered the formation of eutectic melts, i.e. melts that are formed far below the melting point of metallic Zircaloy (~ 2030 K). Oxidation of boron/carbon/zirconium-containing melt led to considerable amount of hydrogen (182 g, 120 g during cooling phase [16]) and to production of CO, CO_2, and CH_4.

6.2. Effective channel approach

The Q-07 bundle test was simulated by the S/Q code using the ‘effective channel approach’ developed earlier [17]. Below the essence of this approach is briefly described.

Since the central rod of the bundle is not heated, its temperature evolution in the course of a quench bundle test is completely determined by thermal-hydraulic boundary conditions: temperatures of the surrounding heated rods and shroud and characteristics of the coolant flow (in the case of Q-07 test – gas mixture velocity and composition). In the case of full-scale simulation of the bundle test the temperatures of the heated rods and shroud are

calculated by specifying the electric power time evolution and thus, the boundary conditions for the central rod are determined by a code. At the same time, there exists another possibility to determine the boundary conditions for the central rod: instead of calculation, the temperatures of the heated rods and shroud may be taken from the experiment.

From the viewpoint of the solution of the heat conduction problem inside the central rod both ways are equivalent. Specification of the boundary conditions on the basis of the experimentally measured temperatures even has certain advantages as it describes the thermal regime around the central rod very close to that in the experiment.

In the S/Q code the thermal boundary conditions for the central rod are predetermined by specifying the temperatures of the "effective channel" inner wall on the basis of experimentally measured temperatures. The inner surface of the effective channel represents the surfaces of the heated rods surrounding the central rod.

The heat exchange between the central rod and the effective channel is affected via radiation and convective heat transfer. The thermal-hydraulic characteristics of the effective channel (cross-section, hydraulic diameter) are determined on the basis of geometrical parameters of the bundle (total cross-section, number of rods and their diameters).

6.3. Processing of the QUENCH-07 bundle test temperature data

During the Q-07 test [14-16] the temperature was continuously measured at different locations of the bundle. 35 thermocouples were attached to the cladding of the heated rods at 17 different elevations between –250 mm and 1350 mm, 3 thermocouples were inserted in the centres of three corner rods at 550, 850 and 950 mm elevations and 3 thermocouples were located between Zr and stainless steel (SS) cladding tubes inside B_4C central rod at 750, 850 and 950 mm. These thermocouples will be referred to below as TFS (Thermo-couple on Fuel rod Simulator).

22 thermocouples were located at the shroud outer surface at 11 different elevations between -250 mm and 1250 mm. Since the TCs were protected by the shroud wall from direct contact with steam, all of them survived throughout the test. These thermocouples will be referred to below as TSH (Thermocouple on SHroud).

The above TCs data were used for simulation of the effective channel internal surface. The numerical procedure of the rod TCs data recalculation includes smoothening, averaging and interpolation (for details of such procedure see [17, 18]). At high elevations the TFS data were used as the basis for the averaged temperature up to the moment of corresponding TC failure, then TSH data were taken as such basis. At lower elevations (below 650 mm) no TC failure occurred, so only TFS data were applied here.

The calculated 'averaged temperature field' describing temperature evolution around central rod was used in the S/Q code input files for the simulation of the quench bundle test Q-07.

At first the imaginary bundle test simulation with the central rod used in the Q-01 – Q-06 tests (Zircaloy-4 cladding and ZrO_2 pellets) and temperature history from the Q-07 test was performed. The main aim of such calculation was to make sure that the real temperature distribution around central rod of the Q-07 test was reproduced correctly. This can be done by comparison of the calculated oxide thickness axial profile with the experimentally measured one. The necessity of such checking is explained by the fact that at high elevations practically all of TFS thermocouples failed long before quenching stage and TSH thermocouples data were used. This leads to rather high uncertainty in the temperature distribution during the hottest period of the test.

After such comparison the 'averaged temperature field' was corrected using the special calculation procedure and the new simulation of the Q-07 test with Zr/ZrO_2 central rod was performed giving much better results with respect to the oxide thickness axial profile. Since

oxidation kinetics strongly depends on the temperature distribution, one may think that the temperature field around central rod is also well reproduced.

The corrected averaged temperature field is presented in Fig. 40.

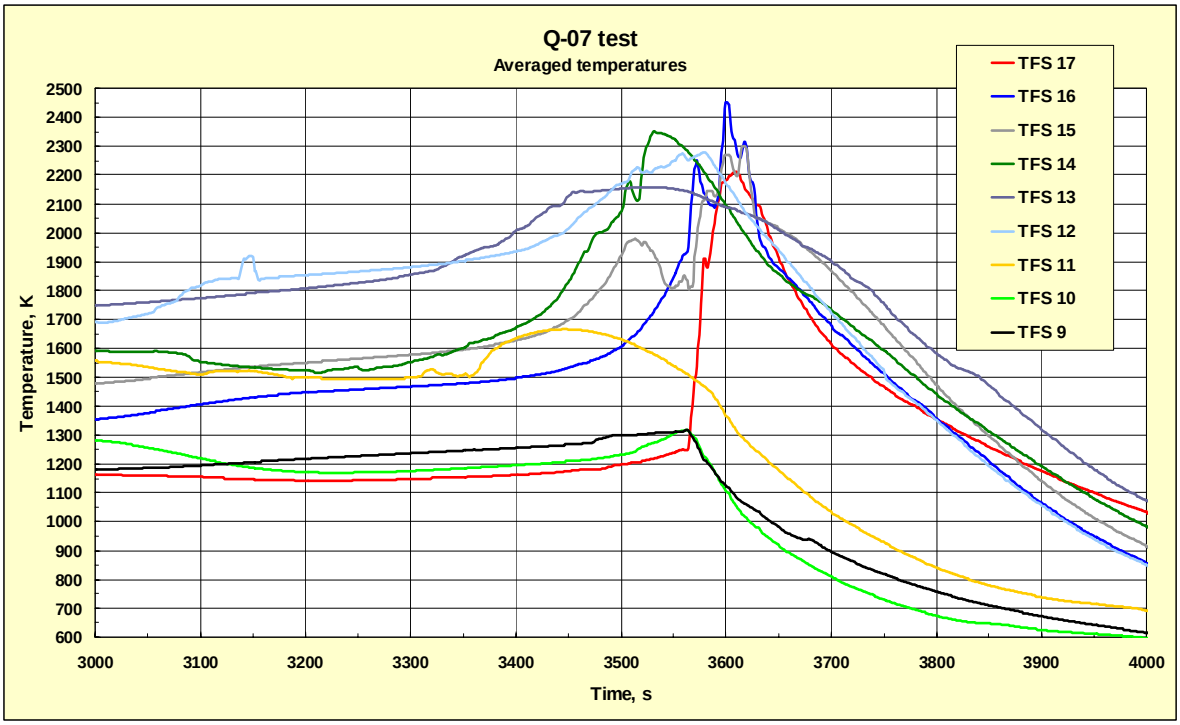

Fig. 40. Corrected average temperature curves. Time interval 3000 – 4000 s.

6.4. QUENCH-07 bundle test simulation with Zr/ZrO_2 central rod

In this bundle test simulation the central rod was assumed to have the same structure as in the Q-01, Q-02, Q-03, Q-04, Q-05, Q-06 and Q-08 tests (Zircaloy-4 cladding and stabilized ZrO_2 pellets). As for the other test conduct parameters (temperature history, inlet gas flow rate, etc.), they were taken from the Q-07 test. In particular, the average temperature field around the central rod shown in Fig. 40 was used as the boundary conditions for the heat exchange problem.

In the S/Q code input files the value of argon inlet flow rate was specified on the basis of FM 401 data (for the description of the QUENCH facility data acquisition system see [14-16]). Since inlet steam flow rate varied significantly during the test, the readings of F 205 (flow rate steam below 10 g/s) from the beginning of the test to the cool-down initiation (3557 s) and F 204 (flow rate steam below 50 g/s) from the cool-down initiation to the end of the test were used directly in the S/Q code input file. Also the reading of T 511 (gas temperature at bundle inlet) was used there.

The bundle nodalization is characterised by the following values:

Heat conduction module

- The total nodes number in the radial direction: 35
- Pellet nodes number in the radial direction: 21

- External layer (oxide) nodes number: 7
- Total nodes number in the vertical direction: 197

The vertical grid used in the heat conduction module is adaptive one, with maximum density in the region of the maximum temperature gradients.

Total number of meshes used by oxidation, mechanical deformation and hydrogen absorption modules was 98. The total central rod length considered was 1975 mm – from the upper point 1500 mm (adjacent to the Al_2O_3 plate thermal shield) to the lower point –475 mm (adjacent to the lower SS plate).

In order to estimate the correctness of the reproduction of the temperature conditions around the central rod, comparison of the calculated oxide thickness axial profile with the experimentally measured one (available at 3090 s when the corner rod was withdrawn from the bundle and at 5526 s (end of the experiment)) was performed.

Quite similar to the other quench bundle tests, the radial temperature distribution inside the bundle was close to uniform during the Q-07 test [14]. Properly speaking, this fact makes it possible to use temperature data of the thermocouples located at different radial positions for description of the temperature field around the central rod. On the other hand, radial temperature uniformity makes the comparison of the calculated central rod oxide thickness with that of the corner rod as well as with the averaged (over all the rods) oxide thickness quite reasonable.

In Fig. 41 the measured oxide layer thickness of the corner rod and the calculated oxide layer thickness of the central rod (3090 s) are presented. One can see rather satisfactory agreement between calculated and experimental data.

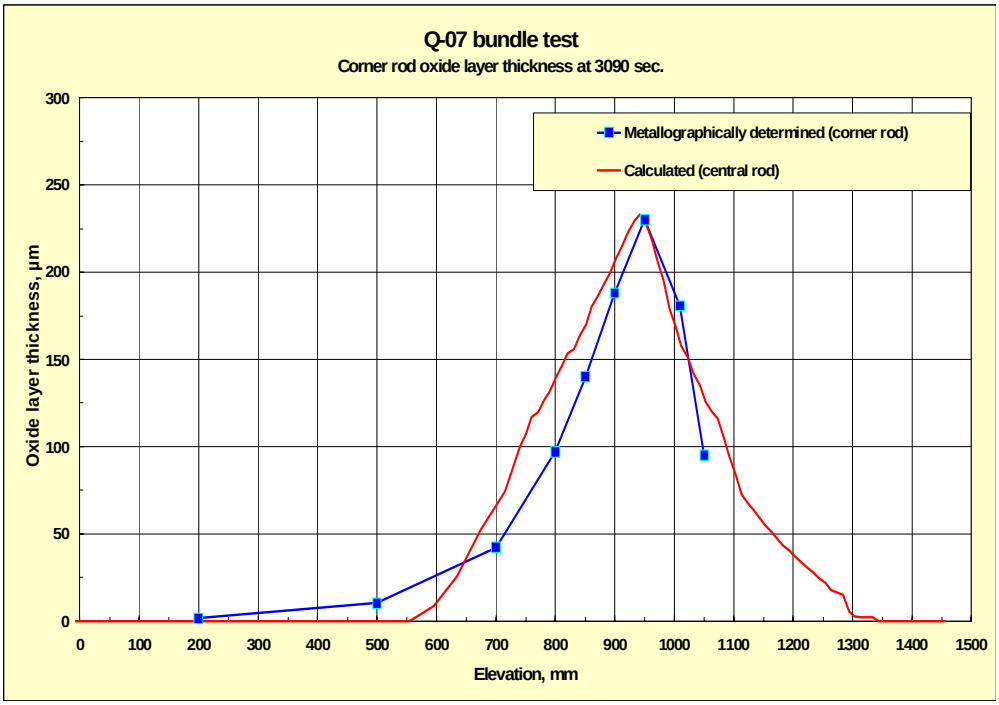

Fig. 41. Oxide layer thickness axial profile of the corner rod B (withdrawn from the bundle at 3090 s) compared to the calculated one of the central rod at 3090 s.

In Fig. 42 the measured oxide layer thickness (averaged over all the rods) and calculated oxide layer thickness of the central rod at the end of the test are presented. Also the calculated oxide layer thickness of the central rod at the moment of cool-down initiation is

given. One can see quite good agreement of the calculated oxide thickness and the measured one. So, it may be concluded that the *temperature regime around the central rod was reproduced quite adequately by the corrected average temperature field*.

Also noticeable is the difference between the calculated oxide thickness at the start of bundle flooding (3564 s) and at the end of the test. Such big difference means that considerable oxidation took place after cool-down initiation. This conclusion generally correlates with the experimental data on hydrogen production.

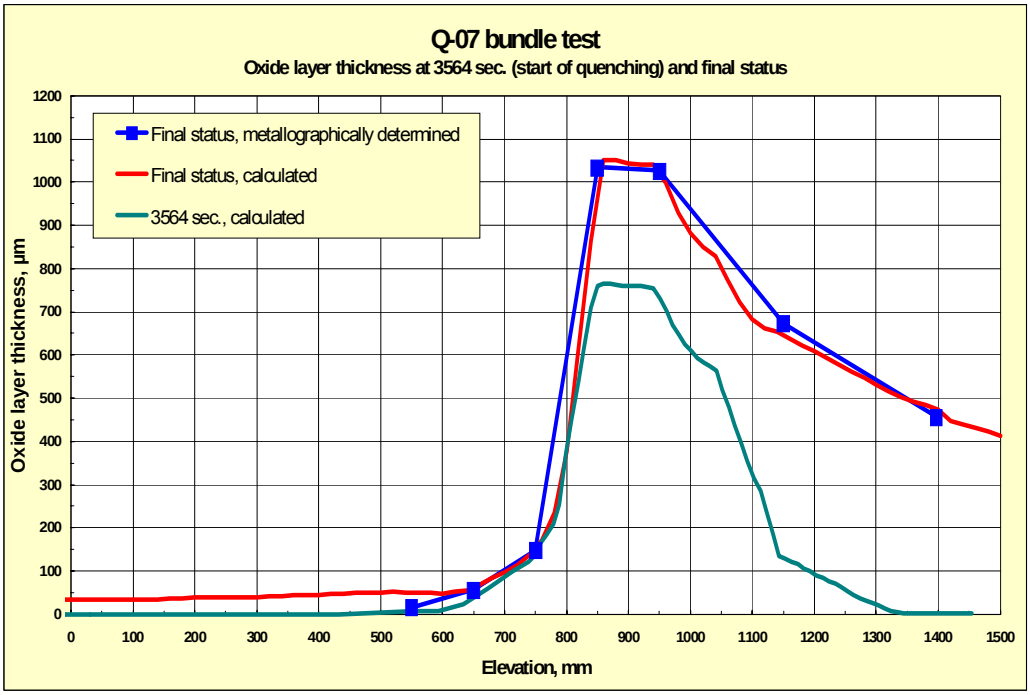

Fig. 42. Measured oxide layer thickness (averaged over the rods, final status), calculated oxide layer thickness of the central rod at 3564 s (start of bundle flooding) and calculated oxide layer thickness of the central rod (final status). Calculation was performed using corrected temperatures.

6.5. QUENCH-07 bundle test simulation with B_4C central rod

With the help of corrected average temperature field, simulation of the Q-07 test with B_4C central rod was performed. Since the model of B_4C-Zr-SS interactions has not been yet implemented in the S/Q code, it was assumed that the cladding was absent and B_4C pellets were exposed to steam flow throughout the whole test. The results of such calculation are presented below[1].

Calculated CO_2, CO and H_2 mass flow rates from the central rod are presented in Fig. 43; calculated B_2O_3, H_3BO_3, HBO_2 mass flow rates are given in Fig. 44. It should be noted here that the calculated mass flow rate values correspond to the temperature of the gas mixture at the bundle outlet. This temperature gradually varied during the test reaching its maximum value of about 2180 K at 3610 s. Chemical composition of the gas mixture strongly depends on temperature and will be quite different at such high temperatures and at working temperature of GAM300 mass spectrometer (110-120°C). Moreover, according to IVTAN-THERMO chemical equilibriums database [6], at temperatures below 500 K boric acids form

[1] The assumption that the B_4C pellets were exposed to steam flow during the whole test is not realistic enough and leads to some overestimation of the 'total carbide release'. The situation can be improved if the time and location of disclosed B_4C pellets will be estimated by a model for B_4C/SS/Zr interaction.

liquid fraction that can clog the pipes leading to MS. Thus, direct comparison of the calculated results with the GAM300 experimental data is not possible.

However, it is possible to compare calculated and experimental data of the total carbide release since the total amount of carbide does not change whatever chemical reactions involving CO_2, CO and CH_4 take place in the gas mixture under consideration.

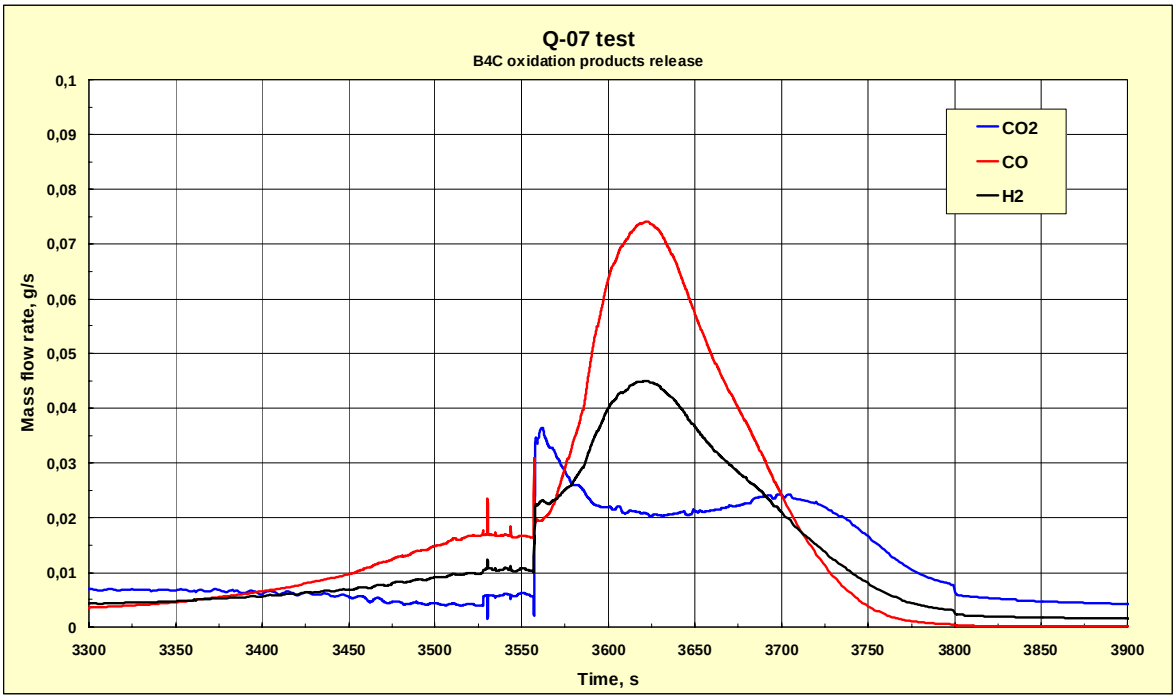

Fig. 43. Calculated CO_2, CO and H_2 mass flow rates.

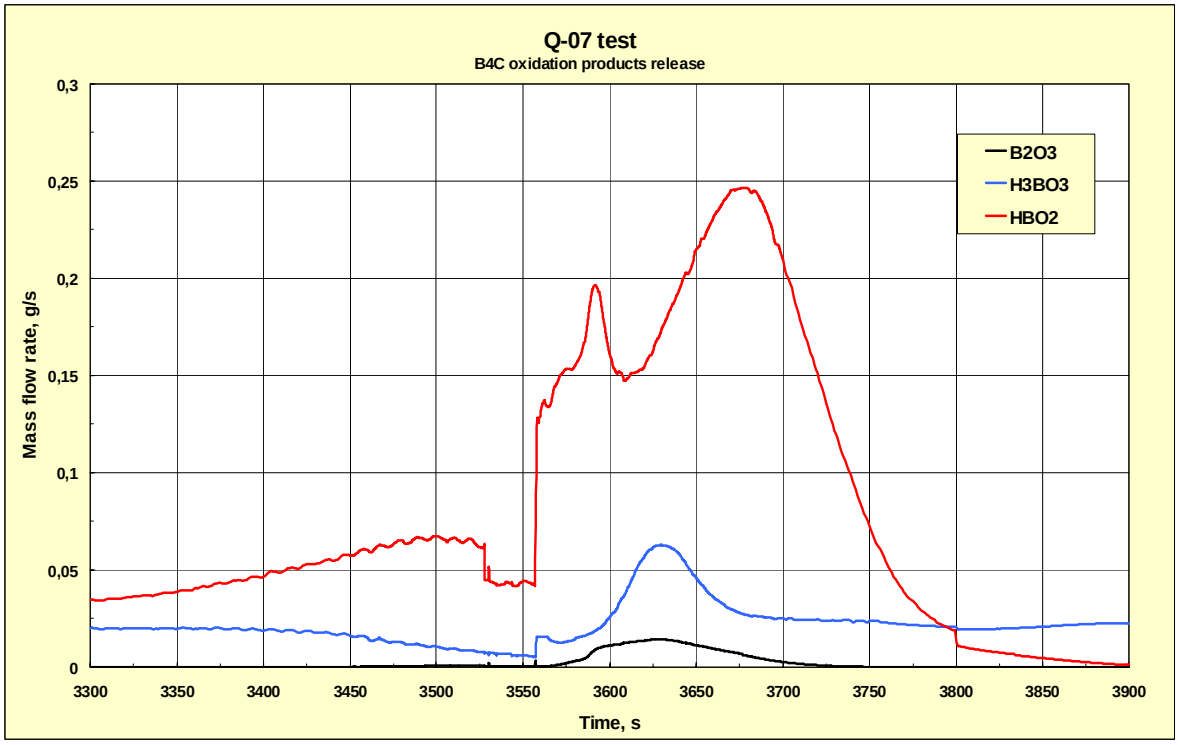

Fig. 44. Calculated B_2O_3, H_3BO_3 and HBO_2 mass flow rates.

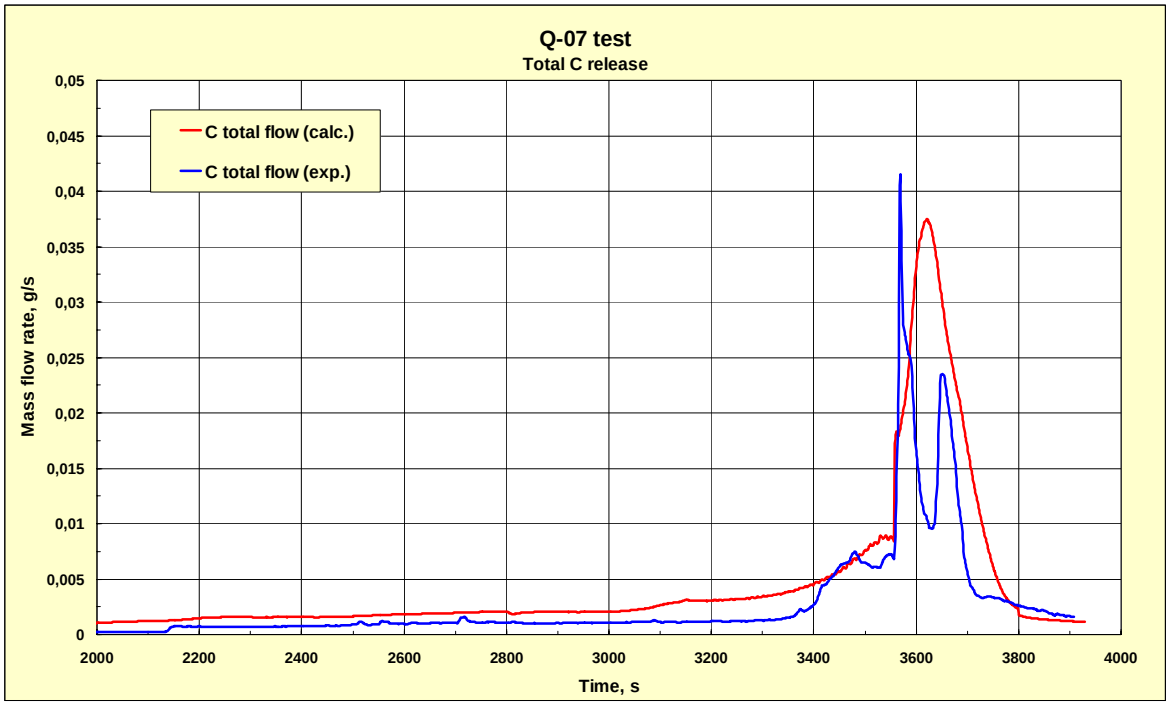

Fig. 45. Experimentally measured and calculated C mass flow rate (in CO_2, CO, CH_4).

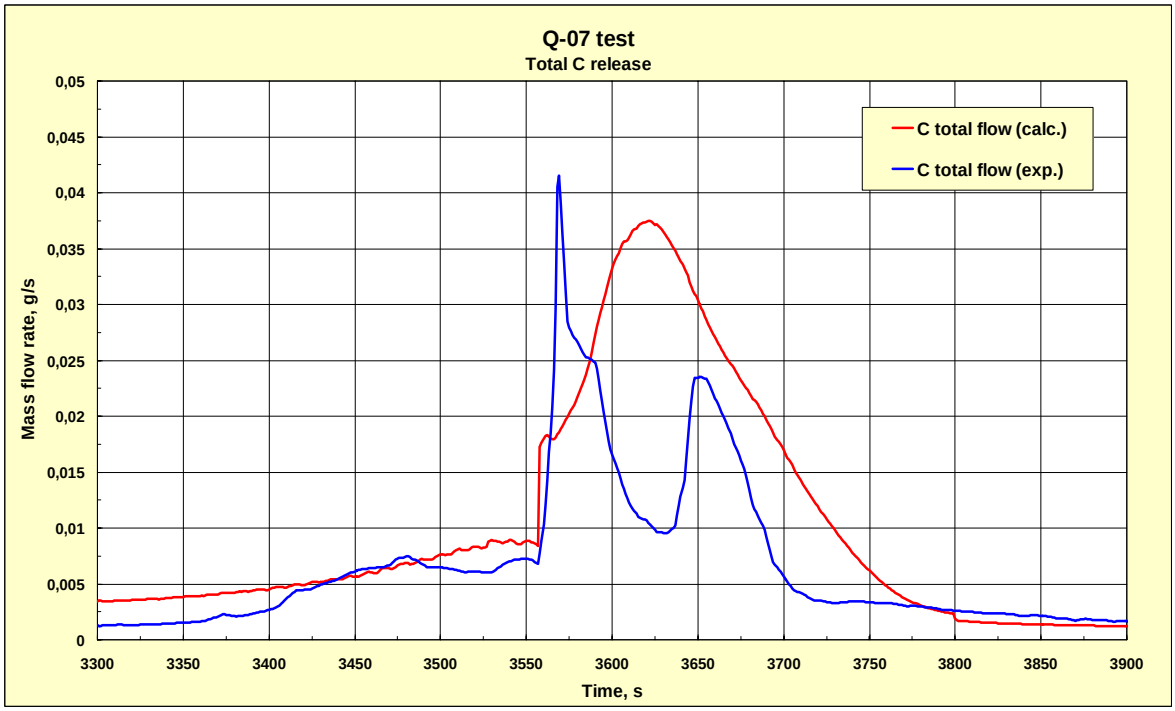

Fig. 46. Experimentally measured and calculated C mass flow rate (in CO_2, CO, CH_4). Time interval 3300 – 3900 s.

By definition,

$$\dot{m}_C = \dot{m}_{CO_2} \frac{M_C}{M_C + 2M_O} + \dot{m}_{CO} \frac{M_C}{M_C + M_O} + \dot{m}_{CH_4} \frac{M_C}{M_C + 4M_H} \tag{60}$$

In Figs. 45 and 46 the experimentally measured and calculated total carbide release estimated in accordance with relation (60) are presented. As one can see, the calculated curve generally correlates well with the experimental one.

Noteworthy is sharp rise of the curves associated with cool-down initiation. According to the B_4C oxidation BOX Rig tests results [1, 19], the oxidation reaction rate is proportional to the steam partial pressure, Eq. (1). On cool-down stage when the steam mass flow rate was increased from 3 g/s to 15 g/s, the partial pressure of steam correspondingly increased resulting in the intensification of B_4C oxidation. This is well reflected by both experimental and calculated curves.

The calculated total amount of different components released by oxidation of B_4C during the test are presented in Table 14.

Component	Total release, g
H_2	12.51
CO_2	17.93
CO	11.76
CH_4	0.00026
B_2O_3	1.31
H_3BO_3	57.63
HBO_2	71.5

Table 14. Total amount of different components released during the test.

As already mentioned, these values cannot be directly compared to the experimental ones since they relate to different temperatures.

The amount of methane is negligibly small; however according to calculations with the IVTAN-THERMO chemical equilibriums software [6] one could expect the increasing of this value at lower temperatures, see Section 5.2.

The amount of released hydrogen is higher than that from the Zr/ZrO_2 central rod (3.942 g), however it is rather small in comparison with the total calculated one (115 g [18]) as well as with the experimental value (182 g).

As for the total carbide production, such comparison is quite possible. The calculated value is 9.94 g and the experimental one is 5.59 g. These values were obtained by integration of the curves presented in Figs. 45 and 46 (mass flow rates calculated according to Eq. (60)) over the test duration. The difference between the calculated and measured carbide amount may be due to oscillations of the experimental curve during temperature escalation phase (Fig. 46). These oscillations seem to be due to still unexplained oscillations of the steam flow rate measured by mass spectrometer GAM 300.

Release of 9.94 g of carbide means that 9.94/12 = 0.828 moles of B_4C was oxidised during the test. Total heat release due to B_4C oxidation (at the pellets surface) may be evaluated using the value of 768 KJ/mol for this reaction [13]:

$$Q_{B_4C} = 768 \cdot 0.828 = 635.5 \text{ (KJ)}. \quad (61)$$

This value should be compared with the total chemical heat release which may be estimated on the basis of the total hydrogen generation of the Q-07 test. The value of 182 g of released hydrogen means 91 atomic moles of oxygen involved in the bundle oxidation. Assuming that the heat effect of bundle oxidation is 300 KJ/mol and neglecting small hydrogen contribution of the B_4C central rod oxidation, one has:

$$Q_{total} = 300 \cdot 91 = 27300 \text{ (KJ)}, \quad (62)$$

i.e. heat release due to B_4C oxidation contributes less than 2.3% of the total heat release.

Thus, one can conclude that neither with respect to hydrogen production nor concerning heat release the B_4C central rod did influence substantially bundle degradation process. One may think that the main effect of B_4C central rod on the bundle behavior is connected with liquid B_4C-Zr and B_4C-SS eutectics formation, their relocation and flow channels blockage. However, description of these effects goes beyond the scope of the present work.

6.6. Main outcomes

The SVECHA/QUENCH code was applied to simulation of the QUENCH bundle test Q-07. The simulation was performed within the framework of the 'effective channel approach' using corrected average temperature field. Data concerning release rate of B_4C oxidation products were analysed.

Direct comparison of the calculated release rates (at the bundle outlet) with the experimentally measured ones (at MS GAM 300 location) is not possible since they correspond to different temperatures. However, this was done for the total carbide release rate which does not depend on temperature value. The calculated carbide release rate generally correlates well with the experimental one but certain discrepancies occur during temperature escalation phase. As a result, calculated amount of produced carbide (9.94 g) is higher than the experimental value (5.59 g).

The total amount of produced hydrogen (12.51 g) is higher than that from the Zr/ZrO_2 central rod (3.942 g), however it is rather small in comparison with total calculated one (115 g) as well as with the experimental value (182 g). The estimated amount of heat released due to B_4C oxidation is also small in comparison with the total chemical heat release (2.3 %). Thus a conclusion can be derived that the main effect of B_4C central rod on the bundle behavior is connected with liquid B_4C-Zr and B_4C-SS eutectics formation, their relocation and flow channels blockage.

7. Conclusions

A new model on B_4C oxidation is developed for analysis of the BOX Rig tests. The model considers the surface reaction kinetics and mass transport in the gas phase as rate determining steps of the oxidation process.

Linear dependence of the reaction rate on the steam surface partial pressure is derived from quantitative analysis of the BOX Rig test results.

An adequate consideration of mass transfer in the gas phase allows correct prediction of measured dependence of oxidation rate on gas flow velocity, also in the tests with invariable steam partial pressure, and predicts increase of such dependence at high temperatures.

A full set of independent chemical reactions is considered in the new B_4C oxidation model. Correspondingly, the full set of mass action laws for equilibrium gas reactions either on the surface or in the gas bulk, is used.

For non-equilibrium surface reactions a semi-empirical correlation for the reaction rate is deduced from the analysis of the BOX Rig test results. In this approach, the main inconsistency of many other B_4C oxidation models (which combine this semi-empirical correlation with the mass action law for the same, non-equilibrium, chemical reaction) is eliminated.

The set of chemical equations is supplemented with flux matches for each gas species, which allows self-consistent conjugation of the chemical reaction rate problem with mass transfer problem in the gas phase.

As a result, a more precise solution for hydrogen release and additionally, a chemical composition of the outlet gas mixture, can be calculated by the advanced model.

The new module of the B_4C oxidation in steam has been implemented in the SVECHA/QUENCH (S/Q) code.

The S/Q code with the newly implemented B_4C oxidation module was verified against the BOX Rig tests. In general, the S/Q code adequately predicts the hydrogen and the carbon dioxide steady-state release rates and very low release rates for carbon monoxide and methane. Additionally, the code predicts a switch from orthoboric acid formation at lower temperature to metaboric acid formation accompanied with direct evaporation of boron oxide at higher temperatures.

New tests are recommended for reduction of experimental uncertainties and comparison with the model predictions. Pre-test calculations for these recommended tests are carried out and presented in the current report.

The SVECHA/QUENCH code was further applied to simulation of the QUENCH bundle test Q-07 with the central absorber B_4C rod. The simulation was performed within the framework of the ‘effective channel approach’ using corrected average temperature field. Data concerning release rate of B_4C oxidation products were analysed.

The calculated hydrogen and carbide release rates generally correlate well with the experimental one but certain discrepancies occur during temperature escalation phase.

The estimated amount of heat released due to B_4C oxidation is small in comparison with the total chemical heat release (2.3%). Thus a conclusion is derived that the main effect of B_4C central rod on the bundle behavior is connected with liquid B_4C-Zr and B_4C-SS eutectics formation, their relocation and flow channels blockage.

The new model might be recommended for implementation in the various integral codes for adequate simulation of the absorber rods oxidation during severe accidents in the NPP. A simplified version of the model has been already implemented in the Russian SA code RATEG/SVECHA and allowed reasonable predictions in plant calculations.

Acknowledgements

This work was supported by Forschungszentrum Karlsruhe under the Contract No. 315/20082306/IMF; the personal support and collaboration of Drs. W. Krauss, G. Schanz and L. Sepold are highly appreciated.

This work was also supported by the Russian Foundation for Basic Research which is greatly acknowledged by the IBRAE authors.

Appendix 1. Justification of a weak dependence of the oxidation rate on diffusion rate in the liquid B_2O_3 layer

In this Appendix a conclusion that the oxidation rate of the B_4C sample during the plateau stage is independent of the B_2O_3 content, which was derived in Section 2.1 from analysis of the BOX Rig tests observations, is qualitatively grounded from the general point of view.

Mass transfer in the reaction system B_4C/steam can be separated in several spatial zones: gas boundary layer, gas/(liquid B_2O_3) interface (consisting of 1-2 atomic layers), liquid B_2O_3 and solid B_4C layers, as schematically represented in Fig. 1-A. The equilibrium state of the system under isothermal conditions is characterised by a constant chemical potential (or partial pressure) for each chemical element across the reaction zones. If the equilibrium state is not attained, a gradient of the chemical potential appears, that is the driving force for the mass transfer in each zone. For example, one can consider variation of the oxygen chemical potential (or partial pressure).

In accordance with the presented in Section 3.1 analysis of the chemical reactions, it is assumed that non-equilibrium chemical reaction steps occurs at the liquid/gas interface, which in this case is also characterised by the chemical potential gradient (drop) across the interface layer. This drop is determined by the difference between the surface μ_s and equilibrium μ_{eq} values of the chemical potential at the interface.

Matching of the diffusion flux in the liquid B_2O_3 to the flux across the interface (i.e. to the chemical reaction rate) takes the form:

$$J_{dif} = \beta\left(\mu_l - \mu_{eq}\right) = \alpha\left(\mu_{eq} - \mu_s\right) = W\,, \qquad \text{(A.1)}$$

where $\beta = \left(D_l/l\right)\partial c/\partial\mu \propto \left(D_l/l\right)$ and D_l is the diffusion coefficient in the liquid oxide layer with the thickness *l*.

From Eq. (A. 1) one obtains:

$$\mu_{eq} = \frac{\beta\mu_l + \alpha\mu_s}{\alpha + \beta}\,, \qquad \text{(A.2)}$$

and

$$J_{dif} = W = \frac{\beta\alpha}{\beta + \alpha}\left(\mu_l - \mu_s\right). \qquad \text{(A.3)}$$

In the case $\beta \sim \alpha$, one can see from Eq. (A.2) that a small variation of β (e.g. owing to variation of *l*) results in a perceptible variation of μ_{eq} and thus, in a variation of the reaction rate $W = \alpha\left(\mu_{eq} - \mu_s\right)$. In the experiment this should be manifested by a noticeable dependence of the oxidation rate *W* on the effective thickness of the oxide liquid layer *l* (which was large in porous pellets and negligible in non-porous ESK pellets, see Section 2.1).

Only in the case $\beta \to \infty$ variation of μ_{eq} calculated from Eq. (A.2) is negligible and the reaction rate $W = \alpha\left(\mu_{eq} - \mu_s\right)$ becomes practically independent on the diffusion barrier thickness *l*, and therefore, a weak dependence of the oxidation rate on sample porosity illustrated in Fig. 1 in Section 2.1 can be properly explained.

It is worthwhile to note that the smaller is the effective thickness of the oxide *l*, the better is approximation of large β (owing to the relationship $\beta \propto l^{-1}$). This may explain a more

perceptible dependence of the oxidation rate on the sample porosity observed in the TG tests [2] at lower temperatures ≤ 800°C, at which the oxide layer thickness increases owing to a relatively strong decrease of the B_2O_3 (direct and/or indirect) evaporation rate.

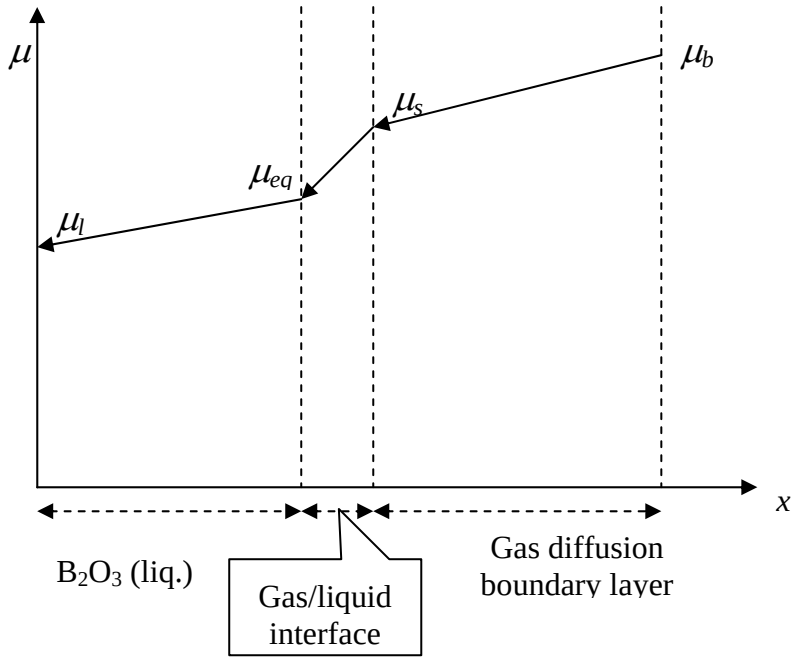

Fig. 1-A. Schematic representation the chemical potential gradient across the reaction zones.

References

1. *M. Steinbrück, A. Meier, U. Stegmaier, L. Steinbock,* Experiments on the Oxidation of Boron Carbide at High Temperatures, FZKA 6979, Forschungszentrum Karlsruhe, Mai 2004

2. *W. Krauss, G. Schanz, H. Steiner*, TG-Rig Tests (Thermal Balance) on the Oxidation of B_4C. Basic Experiments, Modelling and Evaluation Approach, SAM-COLOSS-P027, FZKA 6883, Forschungszentrum Karlsruhe, Oktober 2003.

3. *P. Hofmann, V. Noack, M.S. Veshchunov, A.V. Berdyshev, A.V. Boldyrev, L.V. Matweev, A.V. Palagin, V.E. Shestak*, Physico-Chemical Behavior of Zircaloy Fuel Rod Cladding Tubes During LWR Severe Accident Reflood, FZKA 5846, Forschungszentrum Karlsruhe, Mai 1997.

4. *P. Hofmann, A. Miassoedov, L. Steinbock, M. Steinbrück, A.V. Berdyshev, A.V. Boldyrev, A.V. Palagin, V.E. Shestak, M.S. Veshchunov*, Quench Behavior of Zircaloy Fuel Rod Cladding Tubes. Small-Scale Experiments and Modeling of the Quench Phenomena, FZKA 6208, INV-COBE(98)-D018, Forschungszentrum Karlsruhe, März 1999.

5. *B. Adroguer, F. Bertrand, P. Chatelard, N. Cocuaud, J.P. Van Dorsselaere, L. Bellenfant, D. Knocke, D. Bottomley, V. Vrtilkova, L. Belovsky, K. Mueller, W. Hering, C. Homann, W. Krauss, A. Miassoedov, G. Schanz, M. Steinbrück, J. Stuckert, Z. Hozer, G. Bandini, J. Birchley, T.v. Berlepsch, I. Kleinhietpass, M. Buck, J.A.F. Benitez, E. Virtanen, S. Marguet, G. Azarian, A. Caillaux, H. Plank, A. Boldyrev, M. Veshchunov, V. Kobzar, Y. Zvonarev and A. Goryachev*, *Core loss during a severe accident (COLOSS)*, Nuclear Engineering and Design, Volume 235, Issues 2-4 , February 2005, Pages 173-198.

6. IVTAN-THERMO materials properties database.

7. *A.M. Kutepov, A.D. Polyanin, Z.D. Zapryanov, A.V. Vyazmin, D.A. Kazenin*, Chemical Hydrodynamics (Handbook), Quantum, Moscow 1996.

8. *J.W. Buddenberg, C.R. Wilke*, Ind. Eng. Chem., 41 (1949) 1345.

9. *S. Bretshnayder*, The properties of gases and liquids, Moscow, Chemistry, 1966.

10. *R.C. Reid, J.M. Prausnitz, T.K. Sherwood*, *The properties of gases and liquids*, McGraw-Hill, Inc., New York, 1977.

11. *P.C. Singh and S. Singh*, Int. Comm. Mass Transfer, 10 (1983) 123.

12. SCDAP/RELAP5/MOD2 Code Manual: MATPRO-A Library of Materials Properties for Light-Water-Reactor Accident Analysis. NUREG/CR-5273 EGG-2555, 1990.

13. *I. Barin, O. Knacke*, Thermochemical properties of inorganic substances, Springer Verlag, 1973.

14. *L. Sepold, W. Krauss, A. Miassoedov, D. Piel, U. Stegmaier, M. Steinbrück, C. Homann, S. Horn,* unpublished report, Forschungszentrum Karlsruhe, 2002.

15. *L. Sepold, M. Heck, C. Homann, A. Miassoedov, G. Schanz, U. Stegmaier, M. Steinbrück, J. Stuckert,* unpublished report, Forschungszentrum Karlsruhe, 2003.

16. *M. Steinbrück, C. Homann, A. Miassoedov, G. Schanz, L. Sepold, U. Stegmaier, H. Steiner, J. Stuckert,* Results of the B_4C Control Rod Test QUENCH-07, FZKA 6746, Forschungszentrum Karlsruhe, Mai 2004.

Abstract

A new model on B_4C oxidation in steam at temperatures above 800 °C is developed by the Nuclear Safety Institute of Russian Academy of Sciences, Moscow (IBRAE) based on the analysis of the BOX Rig tests performed at Forschungszentrum Karlsruhe (FZK). The model considers the surface reaction kinetics and mass transport in the gas phase as rate determining steps of the oxidation process.

A full set of independent chemical reactions is considered in the new B_4C oxidation model. Correspondingly, the full set of mass action laws for equilibrium gas reactions either on the surface or in the gas bulk, is used.

For non-equilibrium surface reactions a semi-empirical correlation for the reaction rate is deduced from the analysis of the BOX Rig test results. In this approach, the main inconsistency of many other B_4C oxidation models is eliminated. As a result, a more precise solution for hydrogen release and additionally, a chemical composition of the outlet gas mixture, can be calculated by the advanced model.

The new module of the B_4C oxidation in steam has been implemented in the SVECHA/QUENCH (S/Q) code and verified against the BOX Rig tests.

The SVECHA/QUENCH code was further applied to simulation of the bundle test QUENCH-07 with the central absorber B_4C rod. The simulation was performed within the framework of the 'effective channel approach' using corrected average temperature field. Data concerning release rate of B_4C oxidation products were analysed.

The new model might be recommended for implementation in the various integral codes for adequate simulation of the absorber rods oxidation during severe accidents in the NPP. A simplified version of the model has been already implemented in the Russian SA code RATEG/SVECHA and allowed reasonable predictions in plant calculations.

17. *L. Sepold, P. Hofmann, C. Homann, W. Leiling, A. Miassoedov, D. Piel, G. Schanz, L. Schmidt, U. Stegmaier, M. Steinbrück, H. Steiner, A.V. Palagin, A.V. Boldyrev, M.S. Veshchunov, A.V. Berdyshev, V.E. Shestak*, Investigation of an Overheated PWR-Type Fuel Rod Simulator Bundle Cooled down by Steam (QUENCH-04 test), FZKA 6412, Forschungszentrum Karlsruhe, April 2002.

18. *A.V. Boldyrev, A.V. Palagin, V.E. Shestak*, *M.S. Veshchunov,* Application of the SVECHA/QUENCH code to the simulation of the QUENCH bundle test Q-07, Report IBRAE NSI–SARR–184–04, December 2004.

19. *M. Steinbrück, W. Krauss, G. Schanz, H. Steiner, A.V. Berdyshev, M.S. Veshchunov*, unpublished report, Forschungszentrum Karlsruhe, February 12, 2003.